Dalton Transactions

ROYAL SOCIETY OF CHEMISTRY

PAPER

View Article Online
View Journal | View Issue

Cite this: *Dalton Trans.*, 2023, **52**, 4933

9-Borafluoren-9-yl and diphenylboron tetracoordinate complexes of F- and Cl-substituted 8-quinolinolato ligands: synthesis, molecular and electronic structures, fluorescence and application in OLED devices†

Carina B. Fialho, [a] Tiago F. C. Cruz, [a] Ana I. Rodrigues, [a] Maria José Calhorda, [b] Luís F. Vieira Ferreira, [c] Piotr Pander, [d,e,f] Fernando B. Dias, [f] Jorge Morgado, [g,h] António L. Maçanita [a] and Pedro T. Gomes *[a]

Received 16th February 2023,
Accepted 10th March 2023

DOI: 10.1039/d3dt00496a

rsc.li/dalton

Six new four-coordinate tetrahedral boron complexes, containing 9-borafluoren-9-yl and diphenylboron cores attached to orthogonal fluorine- and chlorine-substituted 8-quinolinolato ligand chromophores, have been synthesised, characterised, and applied as emitters in organic light-emitting diodes (OLEDs). An extensive steady-state and time-resolved photophysical study, in solution and in the solid state, resulted in the first-time report of delayed fluorescence (DF) in solid films of 8-quinolinolato boron complexes. The DF intensity dependence on excitation dose suggests that this emission originates from triplet–triplet annihilation (TTA). Density functional theory (DFT) and time-dependent density functional theory (TDDFT) studies give insight into the ground and excited state geometries, electronic structures, absorption energies, and singlet–triplet gaps in these new organoboron luminophores. Finally, given their highly luminescent behaviour, organic light-emitting diode (OLED) devices were produced using the synthesised organoboron compounds as emissive fluorescent dopants. The best OLED displays green-blue (λ_{EL}^{max} = 489 nm) electroluminescence with an external quantum efficiency (EQE) of 3.3% and a maximum luminance of 6300 cd m^{-2}.

Introduction

Organic light-emitting diodes (OLEDs) are bound by the spin statistics governing charge carrier recombination: only 25% of the created excited states are singlets while the remaining 75% are triplets. In order to overcome the limit imposed by the formation of only 25% singlet excitons upon charge recombination, new strategies involving phosphorescent materials containing iridium and platinum complexes have been explored to allow harvesting of the remaining 75% triplet excitons lost in the electroluminescence process.[1] To this end, the heavy atom effect facilitates intersystem crossing (ISC) *via* a spin–orbit coupling mechanism, thus enabling the use of both singlet and triplet states in emission at room temperature (~100% light emission efficiency). However, relying on emitters containing precious third-row transition-metals may create additional environmental challenges and additional production costs, particularly in industries that may need these materials in large quantities, such as in the display and illumination sectors. Therefore, alternative triplet-harvesting emitters are highly

[a]*Centro de Química Estrutural, Departamento de Engenharia Química, Instituto Superior Técnico, Universidade de Lisboa, Av. Rovisco Pais, 1049-001 Lisboa, Portugal. E-mail: pedro.t.gomes@tecnico.ulisboa.pt*
[b]*BioISI – Instituto de Biossistemas e Ciências Integrativas, Departamento de Química e Bioquímica, Faculdade de Ciências, Universidade de Lisboa, Campo Grande, 1749-016 Lisboa, Portugal*
[c]*BSIRG – Biospectroscopy and Interfaces Research Group, IBB-Institute for Bioengineering and Biosciences, Instituto SuperiorTécnico, Universidade de Lisboa, 1049-001 Lisboa, Portugal*
[d]*Faculty of Chemistry, Silesian University of Technology, Strzody 9, 44-100 Gliwice, Poland*
[e]*Centre for Organic and Nanohybrid Electronics, Silesian University of Technology, Konarskiego 22B, 44-100 Gliwice, Poland*
[f]*Department of Physics, Durham University, South Road, Durham, DH1 3LE, UK*
[g]*Instituto de Telecomunicações, Av. Rovisco Pais, 1049-001 Lisboa, Portugal*
[h]*Department of Bioengineering, Instituto Superior Técnico, Universidade de Lisboa, Av. Rovisco Pais, 1049-001 Lisboa, Portugal*

†Electronic supplementary information (ESI) available. CCDC 2234859–2234863. For ESI and crystallographic data in CIF or other electronic format see DOI: https://doi.org/10.1039/d3dt00496a

desired, such as those containing Earth-abundant metal complexes or those that are fully metal-free luminophores.[2]

Other strategies to harvest both triplet and singlet states involve triplet up-conversion mechanisms to generate delayed fluorescence (DF). This type of emission combines the contribution of both singlet and triplet states. The contribution of triplet states is characterised by the observation of fluorescence lifetimes longer than those of prompt fluorescence (PF), which purely originates from singlet states.[3] There are two main types of up-conversion mechanisms that can result in DF: triplet–triplet annihilation (TTA) and thermally activated delayed fluorescence (TADF).[4] The first route, TTA, occurs predominantly in materials with larger singlet–triplet energy gaps, and is mostly observed in concentrated solutions or at low temperatures when aggregates are formed upon cooling. TTA is also often observed in the condensed phase, where conditions to promote collisions between two triplet species are favoured. In simple terms, these collisions result in the formation of one singlet excited state (S_1) and one singlet ground state (S_0) from two interacting triplet states (T_1): $T_1 + T_1 \rightarrow S_1 + S_0$. The resultant emissive S_1 state decays radiatively to S_0, generating delayed fluorescence. The simple balance of two T_1 states for one S_1 emissive state results in the maximum theoretical internal quantum efficiency (IQE) of TTA-based OLEDs of $25 + \frac{1}{2} \times 75 = 62.5\%$.[5] An alternative to TTA is the aforementioned TADF, which relies on a small S_1–T_1 gap, ΔE_{ST}, usually $\leq$0.2 eV, enabling efficient triplet harvesting by reverse intersystem crossing (RISC), and a maximum theoretical IQE of TADF-based OLEDs of 100%.[4b] Such a small ΔE_{ST} can be achieved by reducing the spatial overlap between the HOMO and LUMO, for example through a popular near-orthogonal donor–acceptor molecular design.[6]

This geometrical requirement can be intrinsically accomplished in neutral tetra-coordinated boron complexes containing monoanionic chelating chromophores, which exhibit tetrahedral geometries about the boron atom. In fact, growing interest in these types of complexes has been recently observed, with numerous luminescent four-coordinate boron complexes being reported in the literature.[7] This appeal is in part due to the low cost and Earth-abundant nature of boron, and to the potential applications of its derivatives, namely in OLEDs. In general, these complexes have the LUMO mostly localised on their π-conjugated chelating ligand, whereas the HOMO may be localised either on the chelating ligand or on the R ancillary ligands (*e.g.* aryls, alkyls, halides) depending on their nature. Their luminescence properties arise from intraligand π–π* electronic transitions and/or charge transfer transitions from the R groups to the orthogonal chelating chromophore. The emission colours can be generally tuned through structural variations on the chelating ligand or R groups, thus affecting the HOMO–LUMO gaps. The observation of DF properties in four-coordinate boron complexes has been relatively rare, including only a restricted number of highly fluorescent complexes exhibiting TADF,[8,9] and an even scarcer number of fluorescent BODIPY derivatives displaying TTA-based delayed fluorescence.[10]

The 8-quinolinolato scaffold has been previously reported with boron complexes, with the very first examples being presented back in 1961 by Douglass,[11] later in 2000 by S. Wang *et al.*,[12] and in 2006 by Slugovc and co-workers.[13] In these studies, boron-bis(aryl) and boron-(phenyl)(alkyl) derivatives (**A** and **B**, Chart 1) were synthesised and their photo- and electroluminescence properties were studied, although DF was not reported. Several authors have also synthesised 8-quinolinolato boron compounds using various boron ancillary ligands, namely by incorporating boron-bis(ethyl) (**C**),[12] substituted -bis(phenyl) (**D**)[14] and -bis(thienyl)[15] (**E**), and 9,10-dihydro-9,10-diboraanthracen-9,10-diyl (**F**)[16] groups, and presented their detailed luminescence studies. However, these experiments recorded in solution have only shown conventional fluorescence. Recently, in the course of this work, Urban, Durka, and co-workers synthesised boron complexes containing the 8-quinolinolato chelating ligand coordinated to the rigid and π-locked 9-borafluoren-9-yl synthon (**G**), also describing their respective structural and photophysical properties.[17] Similarly to the above-mentioned efforts, DF was not reported.

In the present work, we report the synthesis and structural characterisation of a group of new four-coordinate 9-borafluoren-9-yl and diphenylboron fluorescent complexes containing nearly perpendicular 5-fluoro-, 5-chloro- and 5,7-dichloro-8-quinolinolato monoanionic chelating ligands (see Scheme 1) with the aim of altering the electronic nature of the latter fragment, thus evaluating the possibilities of emission colour tuning in these types of compounds. A comparative study of their solution and solid state photophysical features, carried out in steady-state and time-resolved modes, demonstrates delayed fluorescence in the solid state, for the first time in this class of 8-quinolinolato boron complexes. Density functional theory (DFT) and time-dependent density functional theory (TDDFT) studies have been performed to obtain insight into the photoluminescence properties of these new emitters, including the effect of electronegative substituents. Finally, we demonstrate the effective use of our organoboron luminophores in OLEDs with green-blue and green electroluminescence.

Results and discussion

Synthesis and characterisation of boron complexes

The target tetrahedral boron complexes were prepared by coordinating different monoanionic 8-quinolinolato bidentate ligand chromophores to the 9-borafluoren-9-yl and diphenylboron moieties (Scheme 1).

The synthesis of 9-borafluoren-9-yl compounds **3a–d** started by the *in situ* deprotonation of the phenol O*H* protons of the corresponding ligand precursors **1a–d**, using a slight excess of sodium hydride in THF at room temperature. Subsequently, the respective suspension containing the deprotonated ligand precursor was added to 9-chloro-9-borafluorene **2** [18] in THF, at a low temperature, giving rise to the desired products **3a–d**.

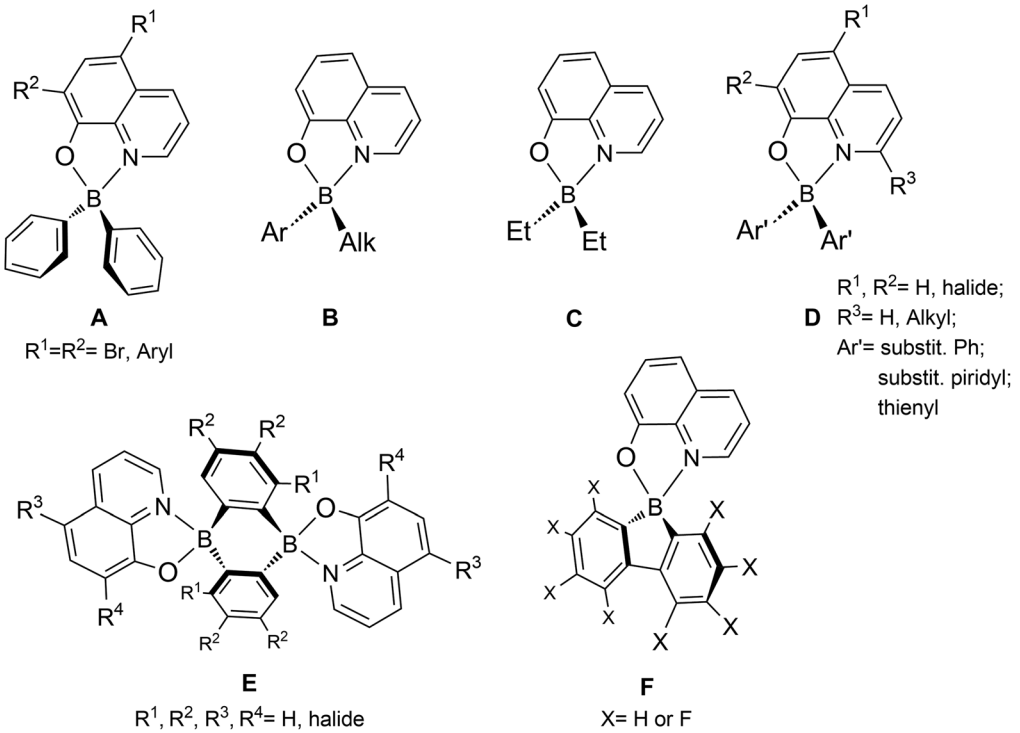

Chart 1 Types of 8-quinolinolato boron complexes reported in the literature.

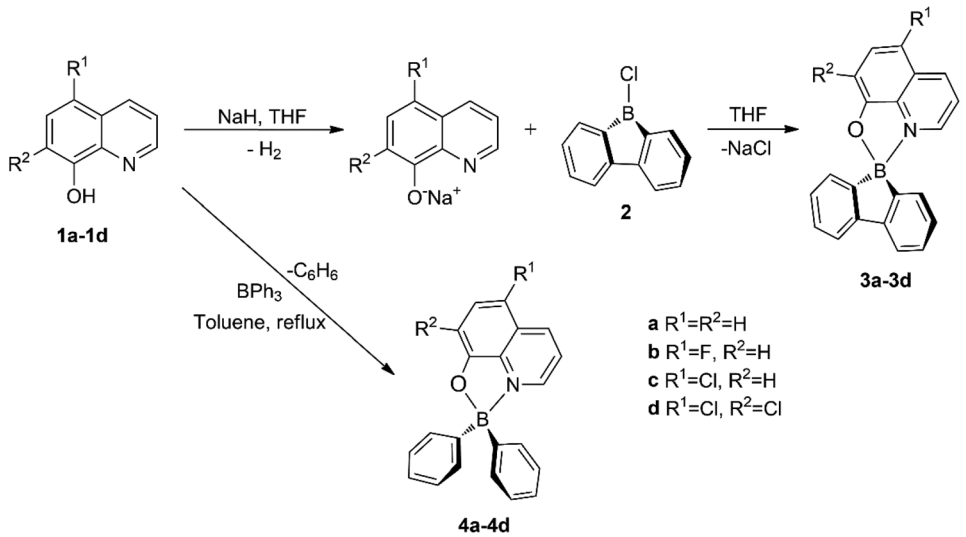

Scheme 1 Syntheses of 9-borafluoren-9-yl (**3a–3d**) and diphenylboron (**4a–4d**) compounds bearing 8-quinolinolato ligands.

The BPh_2 analogue complexes **4a–d** were synthesised as a reference to study the effect of relative molecular rigidity on their optical properties. Complexes **4b–d** were prepared through a modified procedure from that reported for **4a**,[11,12,17] which involved stirring a mixture of the desired 8-quinolinol (*i.e.* 8-hydroxyquinoline) **1a–d** and triphenylboron in toluene under reflux for 16 h.

The 9-borafluoren-9-yl **3a–d** and diphenylboron **4a–d** complexes were obtained in moderate to high yields and were characterised by NMR spectroscopy (^{1}H, ^{13}C, ^{19}F and ^{11}B) – see Fig. S2–S27 in the ESI (ESI†) – elemental analysis and single-crystal X-ray diffraction.

The formation of boron compounds **3** and **4** is evidenced by the absence of O*H* proton resonances in the corresponding ^{1}H NMR spectra, and the appearance of a ^{11}B singlet in the range of δ 3.6–12.9 (three-coordinate ^{11}B resonances occur at chemical shifts higher than 25 ppm (ref. 19)). Concomitantly, the proton and carbon resonances expected for the 8-quinoli-

nolato and 1,1′-biphenyl-2,2′-diyl (complexes **3**) or bis(phenyl) (complexes **4**) moieties were also observed.

Known complexes **3a** and **4a** [13,17] were used as reference compounds for their new halogenated derivatives presented in this work.

X-Ray diffraction studies

The crystal structures of compounds **3b**, **3c**, **3d**, **4b** and **4d** were determined by single-crystal X-ray diffraction. All complexes crystallised in the monoclinic crystal system, in the $P2_1/c$ (complexes **3b**, **3c** and **4b**) and $P2_1/n$ (complexes **3d** and **4d**) space groups. Although the structure of complex **3c** was refined to perfect convergence, the crystal diffracted poorly, and is only presented in Fig. S1 in the ESI† as proof of its molecular connectivity, since its crystallographic information file (CIF) presented A-level alerts. Crystallographic data for these complexes and their most significant bond distances and angles are listed in Table S1 in the ESI.† Perspective views of the corresponding molecular structures of the 9-borafluoren-9-yl (**3b** and **3d**) and bis(phenyl) (**4b** and **4d**) complexes can be seen in Fig. 1.

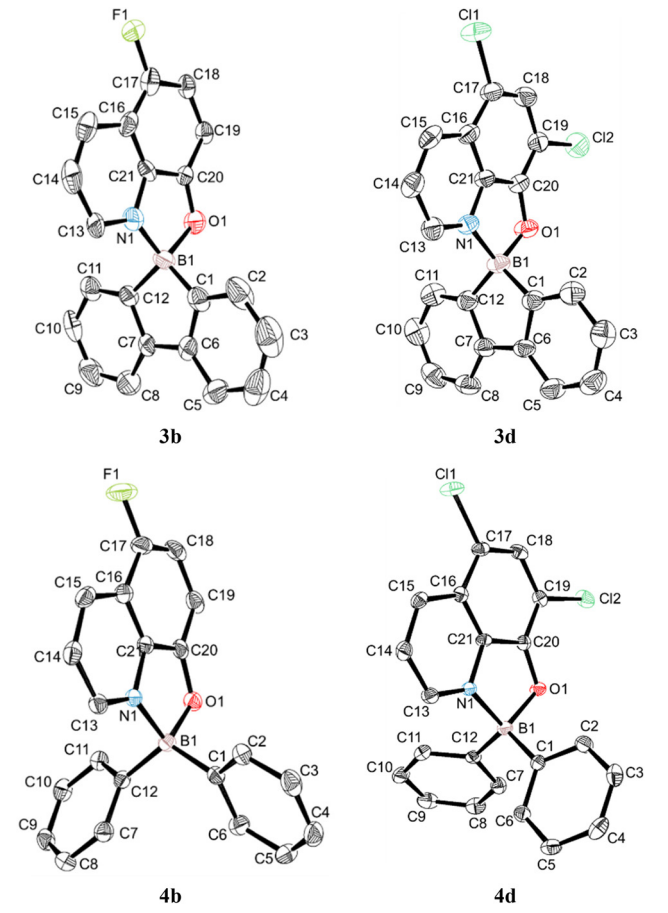

Fig. 1 ORTEP-3 perspective views of the molecular structures of complexes **3b**, **3d**, **4b** and **4d**. The calculated hydrogen atoms have been omitted for clarity and the ellipsoids are drawn at the 50% probability level.

All complexes display boron centres with tetrahedral coordination geometries, containing a bidentate 8-quinolinolato chelate and the 1,1′-biphenyl-2,2′-diyl (complexes **3b**, **3c**, Fig. S1 in the ESI,† and **3d**) or bis(phenyl) (**4b** and **4d**) moieties. Complexes **3b**, **3c**, and **3d** display nearly flat 9-borafluoren-9-yl cores, with the angles between both phenyl rings (defined by the planes containing C1 to C6 and C7 to C12 carbon atoms) being in the range of 3.28(11)–3.85(10)°. The B1–N1 and B1–O1 bond lengths are between 1.592(8)–1.631(3) and 1.517(7)–1.557(8) Å, respectively. The B1–N1, B1–O1, B1–C1 and B1–C12 bonds are nearly identical in group **3** and group **4** complexes. The 8-quinolinolato and 1,1′-biphenyl-2,2′-diyl chelate bite angles differ by *ca.* 2°. The 8-quinolinolato and 9-borafluoren-9-yl cores are nearly orthogonal in all crystallographically characterised complexes **3b**, **3c**, and **3d**, with the angles between the respective bite planes being in the range of 89.08(19)–89.36(10)°. This latter observation is a consequence of the coordination rigidity imparted by the effect of the 9-borafluoren-9-yl unit. By contrast, the C1–B1–C12 bond angles in the bis(phenyl) complexes **4b** and **4d** vary between 116.9(2) and 117.21(16)°, *ca.* 16° larger than those of the 9-borafluoren-9-yl groups, and the phenyl rings are not coplanar. Similar bond lengths and angles have been reported also for other boron 8-quinolinolato complexes.[17,20]

The packing arrangements of complexes **3b** and **3d** are particularly interesting and deserve further discussion. Fig. 2 shows short contacts between adjacent molecules in the crystal packing of complexes **3b** (a) and **3d** (b) and the packing diagram of complex **3d** along the *c* crystallographic axis (c).

In the case of complex **3b** (Fig. 2(a)), there are weak hydrogen bonds between the two molecules in the asymmetric unit. One of the molecules acts as a donor in two interactions: CH···O (2.707 Å) and CH···π (2.532 Å) and as an acceptor in CH···π (2.891 Å) interaction with the other molecule. Other intermolecular interactions between asymmetric units are mainly CH···F (2.414, 2.590 Å) and CH···π (2.820 Å) hydrogen bonds. Some examples of π···π stacking are also observed, but the distances are above 3 Å. When the fluorine atom in **3b** is replaced by a chlorine atom in **3c**, the nature of short contacts changes and the latter is more loosely packed in the solid state.

In complex **3d** (Fig. 2(b)), the CH···O hydrogen bonds (2.550 Å) correspond to the shortest distances in its packing. In the CH···Cl hydrogen bonds (2.713 Å), the H···Cl distance is slightly larger than the H···F one in **3b** (by ~0.3 Å), and longer than the difference in atomic radii between Cl and F (0.28 Å).[21] Considering also that Cl is less electronegative than F, these bonds should be weaker in **3d**. Both Cl···π (3.348 Å) and π···π stacking (3.384 Å) interactions are expected to be weak, as inter-atomic distances appear in the upper range considered for interactions of this type.[22] The molecules of **3d** are packed in the crystal structure forming "X-motifs" defining square prismatic channels with a width equal to 2.393 Å running along the *c* axis (Fig. 2(c)).

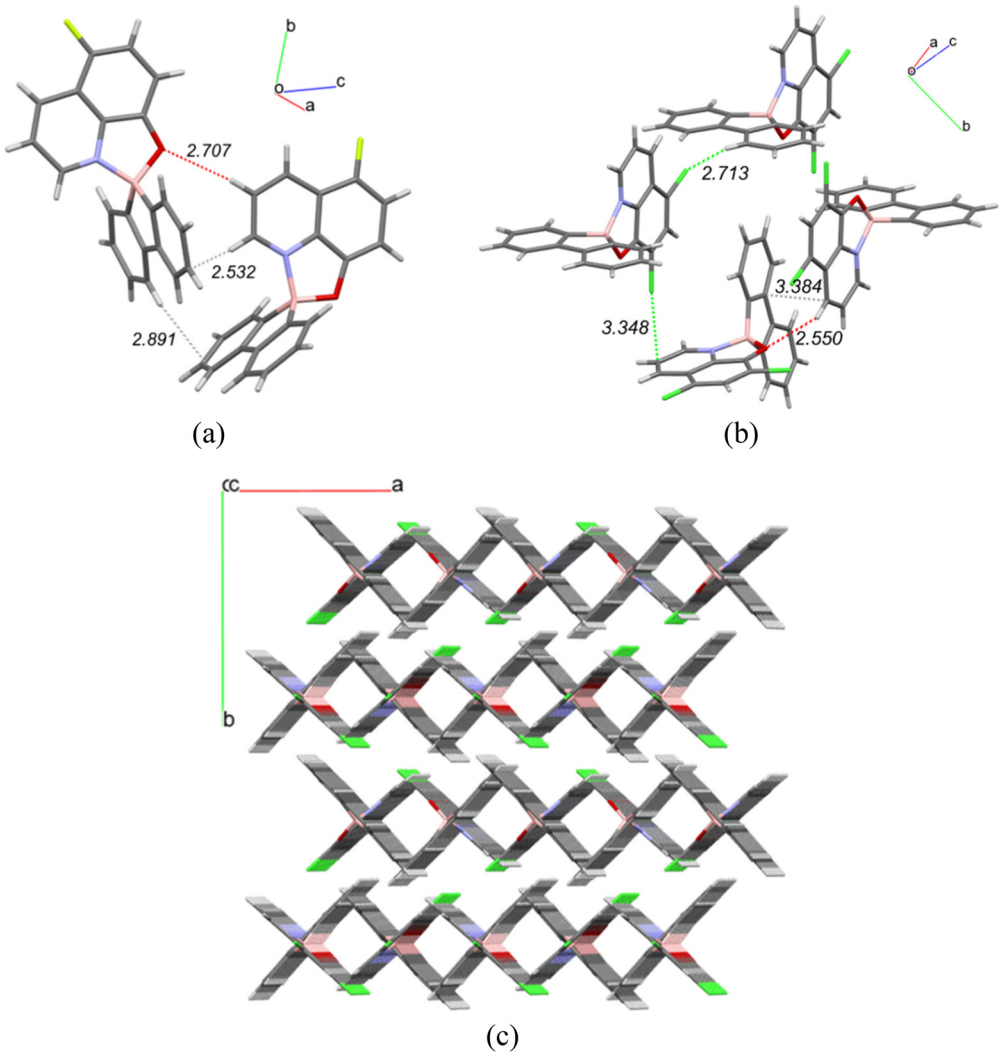

Fig. 2 (a) CH···O and CH···π hydrogen bonds inside the asymmetric unit of **3b**; (b) CH···O, CH···Cl, Cl···π, and π···π stacking between the adjacent molecules of complex **3d**; and (c) packing diagram of the crystal structure of complex **3d** along the *c* crystallographic axis.

Molecular geometries and electronic structures

DFT calculations[23] were performed for the ground state of all 9-borafluoren-9-yl (**3a–3d**) and diphenylboron (**4a–4d**) complexes using the ADF program,[24] considering spin–orbit coupling (SOPERT),[25] with solvent effects included (this is method A used in previous studies; further details including other calculations using B3LYP and BP86 functionals, and also with D3 dispersion corrections, can be found in Computational studies). The geometries of the first excited singlet and triplet states, and the electronic absorption spectra, were calculated using TDDFT.[26]

The rigidity of the 8-quinolinolato ligand introduces a challenge: is there a geometric change between the ground state and the lowest excited singlet and triplet states? Previous studies on related boron complexes[7n–u] demonstrated that 2-iminopyrrolyl ligands undergo a significant distortion, which allows the differentiation of these three electronic states. In **3** and **4**, the distances are always very close to each other and the 8-quinolinolato and 1,1′-biphenyl-2,2′-diyl ligands are rigid, as also found in another study[17] of related 8-quinolinolato boron complexes including the unsubstituted parents **3a** and **4a**.

There is a very good agreement between the calculated bond distances and angles for the ground state geometry and the experimental values from the X-ray data for **3a–3d** and **4a–4d**. The calculated distances and the more relevant angles are collected in Table S2 (ESI†) for complexes **3b** and **3d**, and in Table S3 (ESI†) for **4d**, for easy comparison with the experimental values. The agreement is very good for **3b**, **3d** and **4b**. On the other hand, the optimised geometries of complexes **3a–3d** and **4a–4d** are shown in Fig. S30,† and the bond distances are almost the same when F and Cl atoms are introduced. The bond distances in the series **4a–4d** are very similar, suggesting that the loss of rigidity, when going from the bidentate 1,1′-biphenyl-2,2′-diyl ligand to the two monodentate phenyl ligands, has no influence on them.

The optimised geometries of the first singlet and triplet excited states were obtained from TDDFT calculations as mentioned above. The calculated ground (S_0) and the first excited singlet (S_1) and triplet (T_1) state geometries of **3d** and **4d** are shown in Fig. 3.

The changes in bond lengths are very small (below 0.05 Å), with the shift increasing when going to the S_1 and then to the T_1 states. It is also clear that there is an even smaller difference between the distances in the 1,1′-biphenyl-2,2′-diyl complex **3d** than in the bis(phenyl) derivatives **4b**. These trends are observed for all the complexes **3a–d** and **4a–d** (see Fig. S31–S33† for S_0, S_1, and T_1, respectively). A brief look at the more relevant angles provides a similar picture. The chelation angles O–B–N and C–B–C barely change when going from S_0 to S_1 and T_1: O–B–N shifts between 0.2° and 0.4° in **3**, and between 0.5° and 0.7° in **4**, while the values for C–B–C angles vary from 0.4 to 0.9° (**3**) and 0.5 to 1.0° (**4**). In conclusion, changes in the distances and angles between S_0 and S_1 or T_1 are very small, in contrast to what was observed when 2-iminopyrrolyl ligands bound B in analogous complexes.[7n–t]

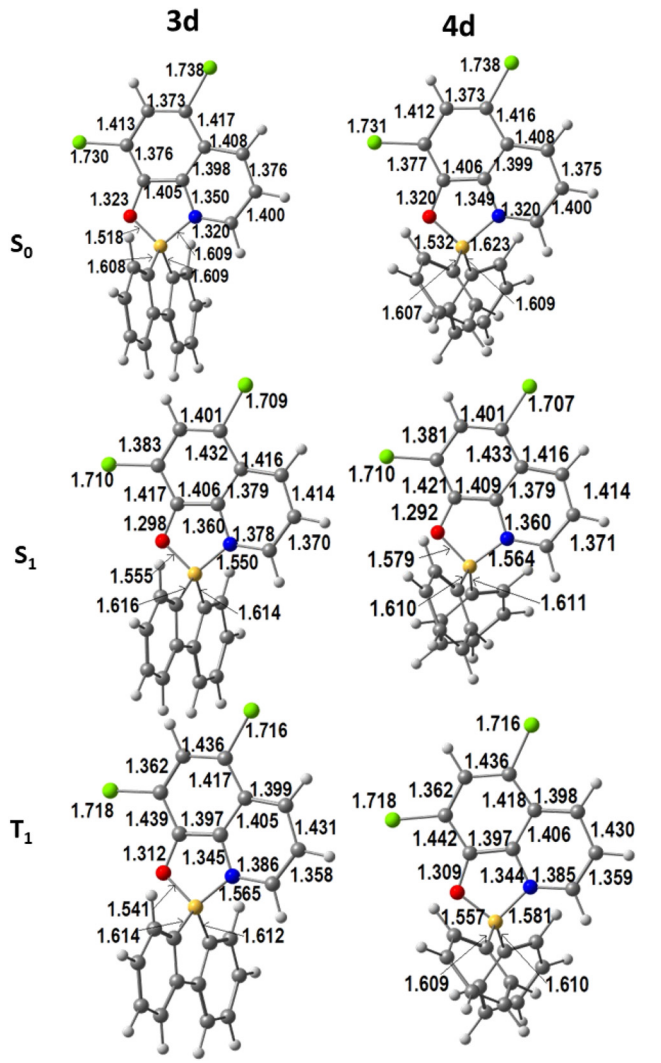

Fig. 3 DFT calculated geometries of complexes **3d** and **4d** in the ground state (S_0) and the first excited singlet (S_1) and triplet (T_1) states (bond lengths in Å).

Photophysical studies: absorption spectra and steady-state fluorescence

The photophysical properties of the 9-borafluoren-9-yl complexes **3a–d** and their BPh_2 analogues **4a–d** were studied in THF solution and in solid state films, dispersed in a ZEONEX 480R cycloolefin polymer. The absorption and fluorescence spectra, and a photograph of their photoluminescence in solution, are shown in Fig. 4 (and also in Fig. S28 in the ESI†).

The absorption and emission wavelength maxima (λ_{abs}^{max} and λ_{em}^{max}) of all complexes in THF solution are within the 393–413 nm and 516–560 nm ranges, respectively (Table 1). The emission colours range from green-blue to green-yellow with increasingly electronegative atom substituents. For ZEONEX 480R films the absorption values are slightly red-shifted (405–424 nm) while the emissions are blue-shifted (502–540 nm). The ε_{max} values of compounds **3a–d** and **4a–d** lay in the range of 4.1–6.2 × 10^3 and 4.4–6.3 × 10^3 L mol^{-1} cm^{-1}, respectively.

When increasing the polarity, from the nonpolar ZEONEX 480R film to the more polar THF, a bathochromic shift is observed in the emission spectra of all complexes **3a–d** and **4a–d**, whereas a hypsochromic shift is noticed in the absorption spectra (see Fig. S28 in the ESI†). This behaviour is attributed to a higher energy stabilisation of the excited state in the emission process, and of the ground state in the absorption process, respectively, with increasing solvent polarity. However, a hypsochromic shift in the absorption spectra is not characteristic of typical π–π* electronic transitions in conventional organic compounds.[27] This result seems not to be determined by changing from the solid state (ZEONEX 480R) to solution, as the same trend is also observed in the absorption spectra of complexes **3a** and **4a** when using solvents of increasing polarity (see Table S4 and Fig. S29, S30 in the ESI†). This effect will be discussed in more detail at the end of the next section.

The fluorescence quantum yields of complexes in THF solutions lay within the range 0.03–0.29. Substitution at position 5 of the 8-quinolinolato ligands with highly electron-withdrawing fluorine clearly leads to a sharp decrease in the fluorescence quantum yields in **3b** and **4b** in relation to the unsubstituted complexes **3a** and **4a** and an increase in the non-radiative rate constants in the former. Substitution with less electronegative chlorines at position 5 (**3c** and **4c**) or positions 5 and 7 (**3d** and **4d**) still leads to a lower photoluminescence quantum yield, but to a less extent than in the F-decorated molecules **3b** and **4b**. Neither F nor Cl (single- or double-) substitutions promote phosphorescence at room or low temperature emission, as clearly seen in the transient emission spectra (see Fig. 6 below in the section Photophysical studies: time-resolved luminescence).

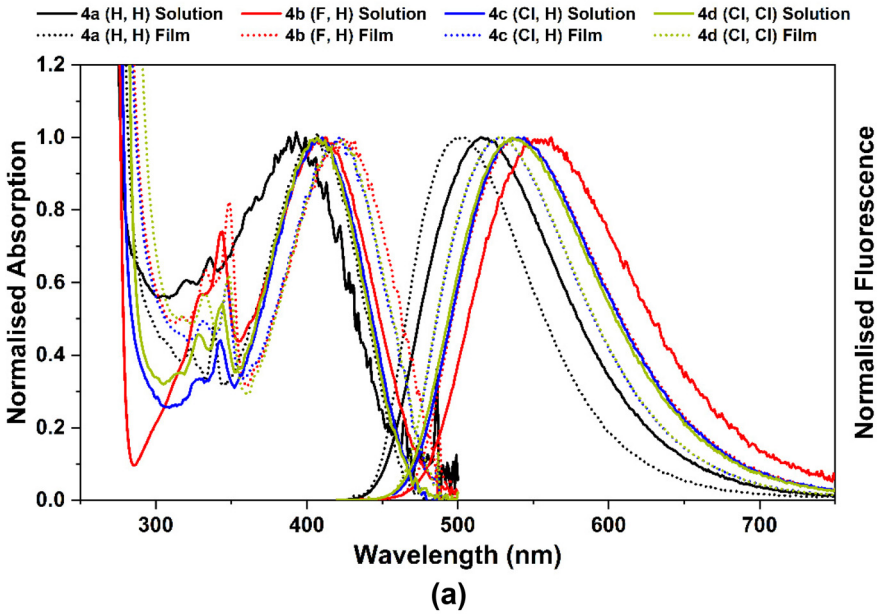

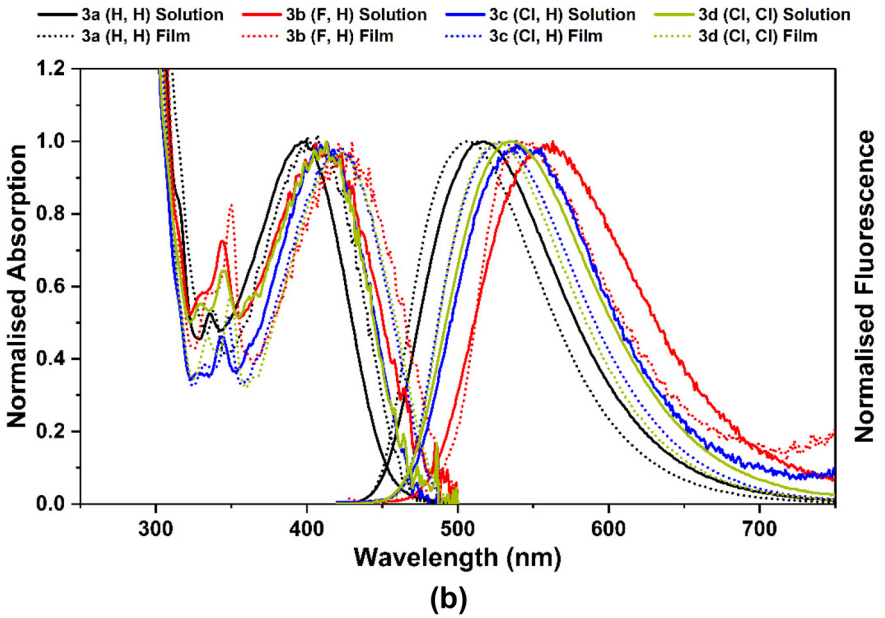

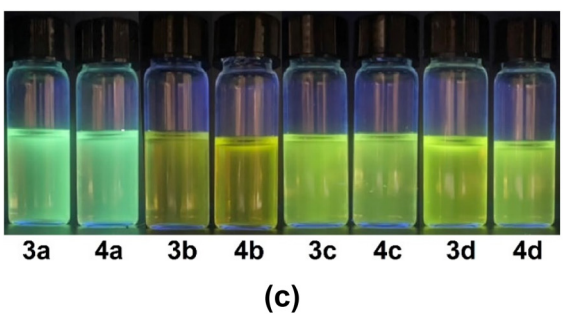

Fig. 4 Normalised absorption and emission spectra of complexes: (a) **4a–d** and (b) **3a–d** in THF solution ($OD_{max} < 0.2$ at λ_{abs}^{max}; $c < 8 \times 10^{-5}$ M) and in films (ZEONEX 480R, 1% wt), at 293 K. (c) Photoluminescence of the respective compounds in THF solution under 365 nm irradiation.

Table 1 Summary of the photoluminescence characteristics of complexes **3a–3d** and **4a–4d** in THF solutions and ZEONEX 480R films, at room temperature (r.t., *ca.* 293 K) and under a N_2 atmosphere

			Solution (THF)							Solid state (ZEONEX 480R film)					
Compound	R^1	R^2	λ_{abs}^{max} [a] (nm)	ε_{max} [b]	λ_{em}^{max} [c] (nm)	Φ_f [d]	τ_f [e,f] (ns)	k_f [g] (ns^{-1})	k_{nr} [h] (ns^{-1})	λ_{abs}^{max} [a] (nm)	λ_{em}^{max} [c] (nm)	Φ_f [d]	τ_f [e] (ns)	k_f [g] (ns^{-1})	k_{nr} [h] (ns^{-1})
4a	H	H	393	5.6	517	0.31	28.1	0.011	0.02	407	502	0.39	28.2	0.014	0.02
3a	H	H	397	5.0	516	0.29	26.3	0.011	0.03	405	506	0.34	27.7	0.012	0.02
4b	F	H	412	4.4	554	0.03	6.1	0.005	0.16	423	539	0.06	10.7	0.006	0.09
3b	F	H	413	4.7	560	0.04	6.0	0.007	0.16	424	540	0.13	9.8	0.013	0.09
4c	Cl	H	409	4.9	539	0.28	13.0	0.022	0.06	422	527	0.25	23.2	0.011	0.03
3c	Cl	H	413	4.1	541	0.25	16.5	0.015	0.05	422	527	0.25	22.2	0.011	0.03
4d	Cl	Cl	407	6.3	535	0.27	21.7	0.012	0.03	422	527	0.26	23.8	0.011	0.03
3d	Cl	Cl	411	6.2	535	0.19	16.3	0.012	0.05	422	525	0.21	20.1	0.010	0.04

[a] Absorption wavelength maxima (λ_{abs}^{max}). [b] Molar extinction coefficients (ε_{max}), 10^3 L mol^{-1} cm^{-1}. [c] Photoluminescence wavelength maxima (λ_{em}^{max}). [d] Fluorescence quantum yields (Φ_f). [e] Fluorescence lifetimes (τ_f). [f] From single exponential decays. [g] Radiative rate constants (k_f); $k_f = \Phi_f/\tau_f$. [h] Sum of non-radiative rate constants (k_{nr}).

TDDFT calculation of electronic transitions and excited state energy

To obtain insight into the electronic properties of complexes **3a–d** and **4a–d**, TDDFT calculations, including spin–orbit coupling and using THF as a solvent, were also performed to determine the absorption spectra and the energies of the first excited singlet and triplet states. The relevant frontier molecular orbitals needed to analyse the spectra and their energies are shown in Fig. 5 for **3c**, **3d**, and **4d** and in Fig. S34 (ESI†) for the remaining complexes. The energies of HOMOs and LUMOs determined by DFT (all methods used) for complexes **3a–d** and **4a–d** are given in Table S5 (ESI†).

The calculated values for the lower energy $S_0 \rightarrow S_1$ absorptions for all the complexes (Table 2) reproduce very well the experimental values (Table 1). The largest difference is 17 nm for **3a** and the smallest difference is 6 nm for **4d**. The lower energy absorption band of **3a** ($S_0 \rightarrow S_1$, calculated at 380 nm) results from two excitations from the HOMO and HOMO−1 to the LUMO. While the LUMO is completely localised in the 8-quinolinolato ligand, the HOMO is essentially located in the 1,1′-biphenyl-2,2′-diyl ligand, and the HOMO−1 includes both the ligands. This absorption involves both a charge transfer from the 1,1′-biphenyl-2,2′-diyl to the 8-quinolinolato ligand and an intraligand (IL, 8-quinolinolato) π–π* component. With the introduction of fluorine or chlorine in **3b** or **3c**, the LUMO remains in the 8-quinolinolato moiety while the HOMO and the HOMO−1 are delocalised over the two bidentate ligands with a small contribution of F or Cl atoms. The nature of the $S_0 \rightarrow S_1$ transition is therefore similar to the one in **3a**. In complex **3d**, with two Cl substituents, the LUMO maintains the same localisation in the 8-quinolinolato ligand, but both the HOMO and HOMO−1 are almost completely localised in the 1,1′-biphenyl-2,2′-diyl ligand. Therefore, the HOMO → LUMO and HOMO−1 → LUMO transitions ($S_0 \rightarrow S_1$) display a charge transfer character (both interligand, 1,1′-biphenyl-2,2′-diyl to 8-quinolinolate).

The calculated emission energies presented in Table 2 match very well the experimental data in Table 1. The energies of the T_1 state are also included in Table 2, together with the fluorescence radiative rate constants defined as $k_f = 1/\tau$, where τ is the calculated lifetime of the S_1 state. The calculated values of k_f are comparable with the experimental rate constants. The ΔE_{ST} of complexes **3a–d** and **4a–d** is close to ~1 eV and hence disqualifies TADF as a potential DF mechanism.[6] As mentioned in the Introduction section, the ΔE_{ST} observed in typical TADF complexes is usually <0.2 eV,[4b] which is significantly lower than the value calculated for our luminescent systems. Indeed, to obtain a computational reference for this statement, TDDFT calculations were performed using the same methodology (see Computational studies in the Experimental section) in boron related systems that were reported to display TADF.[8c] The energy differences between the first singlet and triplet states in those systems are *ca.* 0.05 eV.[28]

To examine the above-mentioned observed shifts of absorption and emission maxima, namely the hypsochromic shift between the nonpolar ZEONEX 480R film (ε = 2.34 [29]) and the more polar THF, the absorption spectra were calculated either in vacuum (nonpolar) or using a solvent model (THF, ε = 7.58 contained in ADF[24]) to simulate the solvation effects of a more polar medium. As shown in Table S6 (ESI†), the calculated lowest energy absorption values lay very close to the experimental results. For instance, the experimental λ_{max} in ZEONEX 480R is 407 while the calculated value is 402 nm for **4a**, similarly for **3a** the values are 405 and 398 nm, respectively. The calculated dipole moments of the S_0 structures **3** and **4** vary from 5.79 D in **4c** to 8.10 D in **3a** (all the dipole moments are collected in Table S6 in the ESI†). After the vertical excitation to the singlet state and before geometrical reorganisation of the molecule, *i.e.* in the non-relaxed Franck–Condon excited state S'_1, they all decrease (values between 4.30 D in **3b** and 6.08 D in **4a**), namely 5.05 D for **4c** and 5.98 D for **3a**. Since the ground state is more polar than the excited state, it is energetically more stabilised than the excited state with increasing polarity, therefore explaining the observed absorption shifts to the blue region. The dipole moments increase after the reor-

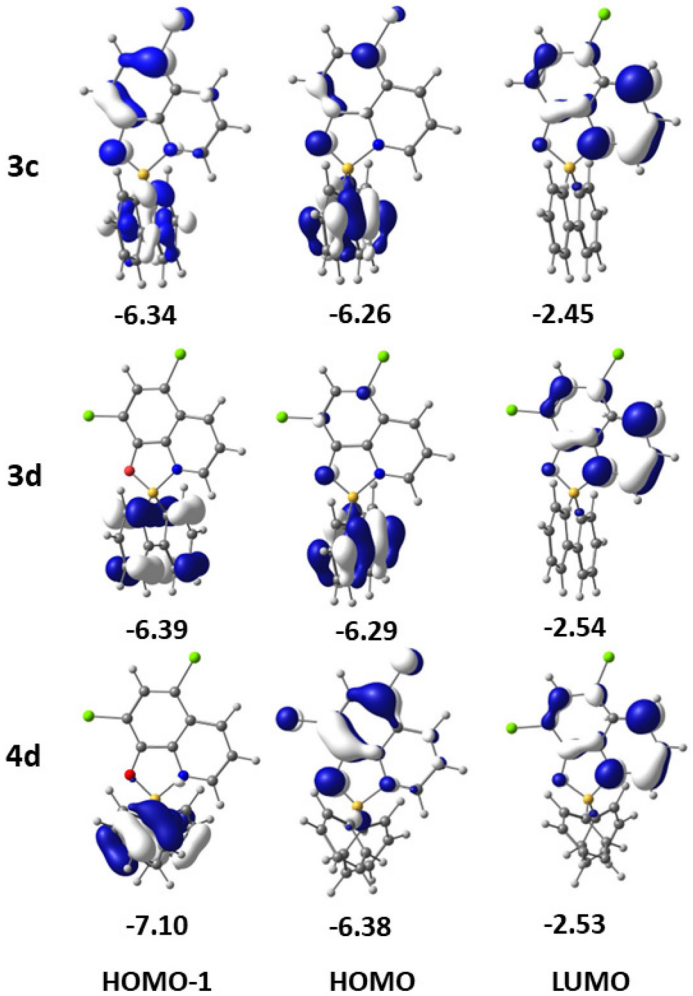

Fig. 5 Frontier molecular orbitals (HOMO–1, HOMO and LUMO) of complexes **3c**, **3d**, and **4d**, with their energies in eV.

Table 2 Comparison between the DFT-calculated and experimental photophysical properties of boron complexes **3a–d** and **4a–d**: absorption (λ_{abs}^{max}) and emission maxima (λ_{em}^{max}) in THF, fluorescence radiative rate constants (k_f), and calculated triplet state energy (T_1)

			λ_{abs}^{max}		λ_{em}^{max}		k_f		T_1
Compound	R^1	R^2	Exp. (nm)	Calc. (nm)	Exp. (nm)	Calc. (eV, nm)	Exp. (ns^{-1})	Calc. (ns^{-1})	Calc. (eV, nm)
4a	H	H	393	383	517	2.49 (498)	0.011	0.067	1.54 (805)
3a	H	H	397	380	516	2.49 (498)	0.011	0.034	1.53 (810)
4b	F	H	412	399	554	2.26 (549)	0.005	0.054	1.35 (918)
3b	F	H	413	401	560	2.27 (546)	0.007	0.043	1.35 (918)
4c	Cl	H	409	400	539	2.31 (537)	0.022	0.070	1.41 (879)
3c	Cl	H	413	399	541	2.31 (537)	0.015	0.045	1.41 (879)
4d	Cl	Cl	407	401	535	2.31 (537)	0.012	0.061	1.43 (867)
3d	Cl	Cl	411	400	535	2.32 (534)	0.012	0.025	1.43 (867)

ganisation of the singlet excited state (relaxed excited state S_1), with values ranging from 5.96 D in **4c** to 8.81 D in **3a**. This increase in polarity is associated with the red shift of the emission energies detected when increasing the polarity of the solvent owing to a higher energy stabilisation of S_1 in relation to S_0.

Photophysical studies: time-resolved luminescence

The selected transient emission spectra of complexes **3a,d** and **4a,d** in ZEONEX 480R films (1% wt), at room temperature and at 77 K, are shown in Fig. 6. The remaining spectra of **3b,c** and **4b,c** are presented in the ESI (Fig. S35†).

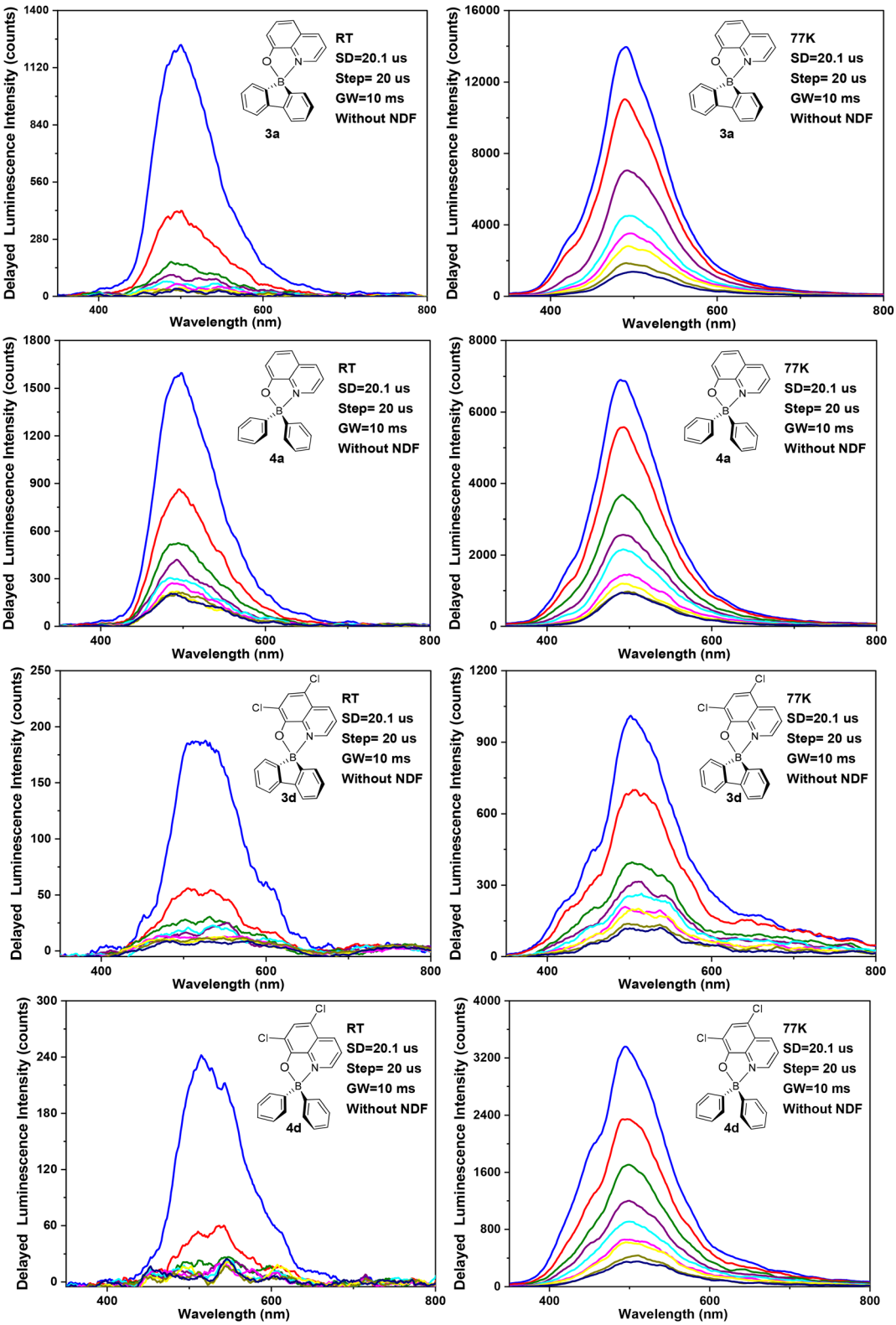

Fig. 6 Transient emission spectra of complexes **3a,d** and **4a,d** in ZEONEX 480R films (1% wt) at room temperature (*ca.* 293 K) (left) and at 77 K (right). All spectra were recorded with a start delay (SD) of 20.1 μs (blue curve) and with a delay increment of 20 μs (step), with the use of a large gate width (GW = 10 ms). The delayed fluorescence intensity decreases at each delay increment.

Table 3 Delayed fluorescence lifetimes (τ_{DF}) and emission maxima for boron complexes **3a–d** and **4a–d**, at r.t. and 77 K, in solid state ZEONEX 480R films

			PF[a]		DF[b]			
			r.t.[c]		r.t.[c]		77 K	
Compound	R^1	R^2	λ_{em}^{max} [d,e] (nm)	τ_f [a,e] (ns)	λ_{em}^{max} (nm)	τ_{DF} [f] (μs)	λ_{em}^{max} (nm)	τ_{DF} [f] (μs)
4a	H	H	502	28.2	499	29	491	58
3a	H	H	506	27.7	499	61	492	64
4b	F	H	539	10.7	542	n.d.[g]	492	32
3b	F	H	540	9.8	542	17	529	55
4c	Cl	H	527	23.2	522	n.d.[g]	499	29
3c	Cl	H	527	22.2	523	13	520	42
4d	Cl	Cl	527	23.8	519	13	503	74
3d	Cl	Cl	525	20.1	525	14	507	42

[a] PF: prompt fluorescence. [b] DF: delayed fluorescence. [c] r.t. = *ca.* 293 K. [d] Steady-state fluorescence. [e] Data reproduced from Table 1. [f] τ_{DF} values were estimated from the half-life of photoluminescence decay obtained from the transient emission spectra, thus divided by ln(2). [g] Not determined, due to a low signal-to-noise ratio.

Table 3 lists the corresponding delayed fluorescence emission spectrum maxima along with the calculated delayed fluorescence lifetimes (τ_{DF}), at room temperature and at 77 K. The minimal delay time of *ca.* 20.1 μs used in the transient photoluminescence experiments in Fig. 6 and S35† eliminates the possibility of detecting prompt fluorescence (PF). Most of the complexes display delayed fluorescence in ZEONEX 480R films, both at room temperature and at 77 K. Delayed fluorescence quenching caused by oxygen was not observed as air- and argon-equilibrated samples display the same properties. This behaviour indicates that the diffusion of O_2 in the polymer films is negligible and thus it does not quench the triplet states involved in the delayed emission process (at least under the conditions and in the timescales used in the experiments).

The observed emission intensities at 77 K are significantly higher than those recorded at room temperature. This behaviour is in line with the expected reduction of non-radiative decay of the triplet state T_1 contributing to the observed delayed fluorescence. Further studies of delayed emission intensity as a function of excitation dose clarify the nature of this long-lived photoluminescence and are presented in Fig. 7 for complexes **3a,d** and **4a,d**. By fitting the experimental data in the log–log scale, a linearised form of the general relationship $Y = aX^b + c$ is used, where Y = DF intensity, X = excitation dose, and a, b, c are constants.

In the fit presented in Fig. 7, 'slope' is interpreted as exponent b in the equation above. For intramolecular processes, such as TADF, $b = 1$, while for a process involving two excited states, such as TTA, $b = 2$ is expected. A value of $b \approx 2$ is observed for all four complexes studied: **3a,d** and **4a,d**, reflecting a clear quadratic dependence of the delayed luminescence intensity on the concentration of excited species, in accordance with the bimolecular nature of the TTA process occurring in these solid state samples.[6b]

Electroluminescence studies

A series of OLEDs were produced using complexes **3a**, **4a**, **3c**, **4c**, **3d**, and **4d** as the emissive dopants to study the effect of halogenation of the emitter on the electroluminescence properties of the device. The summarised characteristics of all OLED devices are presented in Table 4 and Fig. 8. Supplementary figures are provided in the ESI (Fig. S36–S38†). Device codes follow emitter names with the exception of **3a opt**. and **4a opt**., which denote the optimised variants of devices **3a** and **4a**.

At first, a study of the differences between linked and separated phenyl ligands in devices **3a** and **4a** was attempted with the following general structure (Fig. S39 in the ESI†): ITO | HAT-CN (10 nm) | TSBPA (40 nm) | mCP (2 nm) | mCP co 10% emitter (20 nm) | PO-T2T (5 nm) | TPBi (40 nm) | LiF (0.8 nm) | Al (100 nm). Here HAT-CN {dipyrazino[2,3-*f*:2′,3′-*h*]quinoxaline-2,3,6,7,10,11-hexacarbonitrile} served as the hole injection layer, while TSBPA {4,4′-(diphenylsilanediyl)bis(*N*,*N*-diphenylaniline)} served as the hole transport layer. A thin layer of mCP {1,3-bis(carbazol-9-yl)benzene} served as an additional hole transport layer and exciton blocking layer. mCP also served as the host material in the emissive layer. PO-T2T {2,4,6-tris[3-(diphenylphosphinyl)phenyl]-1,3,5-triazine} served as the hole blocking layer, while TPBi {1,3,5-tris(1-phenyl-1*H*-benzimidazol-2-yl)benzene} served as the electron transport layer. LiF was the electron injection layer and Al served as the cathode. Devices **3a** and **4a** have demonstrated comparable properties with the maximum external quantum efficiency (EQE) of ~2.5% and near identical electroluminescence spectra (Fig. 8 and Table 4). The maximum luminance of device **3a** (3600 cd m^{-2}) was, however, larger than that of **4a** (2600 cd m^{-2}). We have attempted to further optimise the structure of devices **3a**/**4a** by introducing an electron-transport layer PO-T2T into the emissive layer, which resulted in devices **3a opt**. and **4a opt**. (Fig. S40 in the ESI†). The OLED architecture of **3a**/**4a opt**. is similar to that of **3a**/**4a**, but the emissive layer comprises a blend of mCP and PO-T2T:[30,31] ITO | HAT-CN (10 nm) | TSBPA (40 nm) | mCP (2 nm) | mCP : PO-T2T (80 : 20) co 10% emitter | PO-T2T (5 nm) | TPBi (40 nm) | LiF (0.8 nm) | Al (100 nm). Devices **3a opt**. and **4a opt**. display enhanced electroluminescence characteristics, which can be attributed to an improved

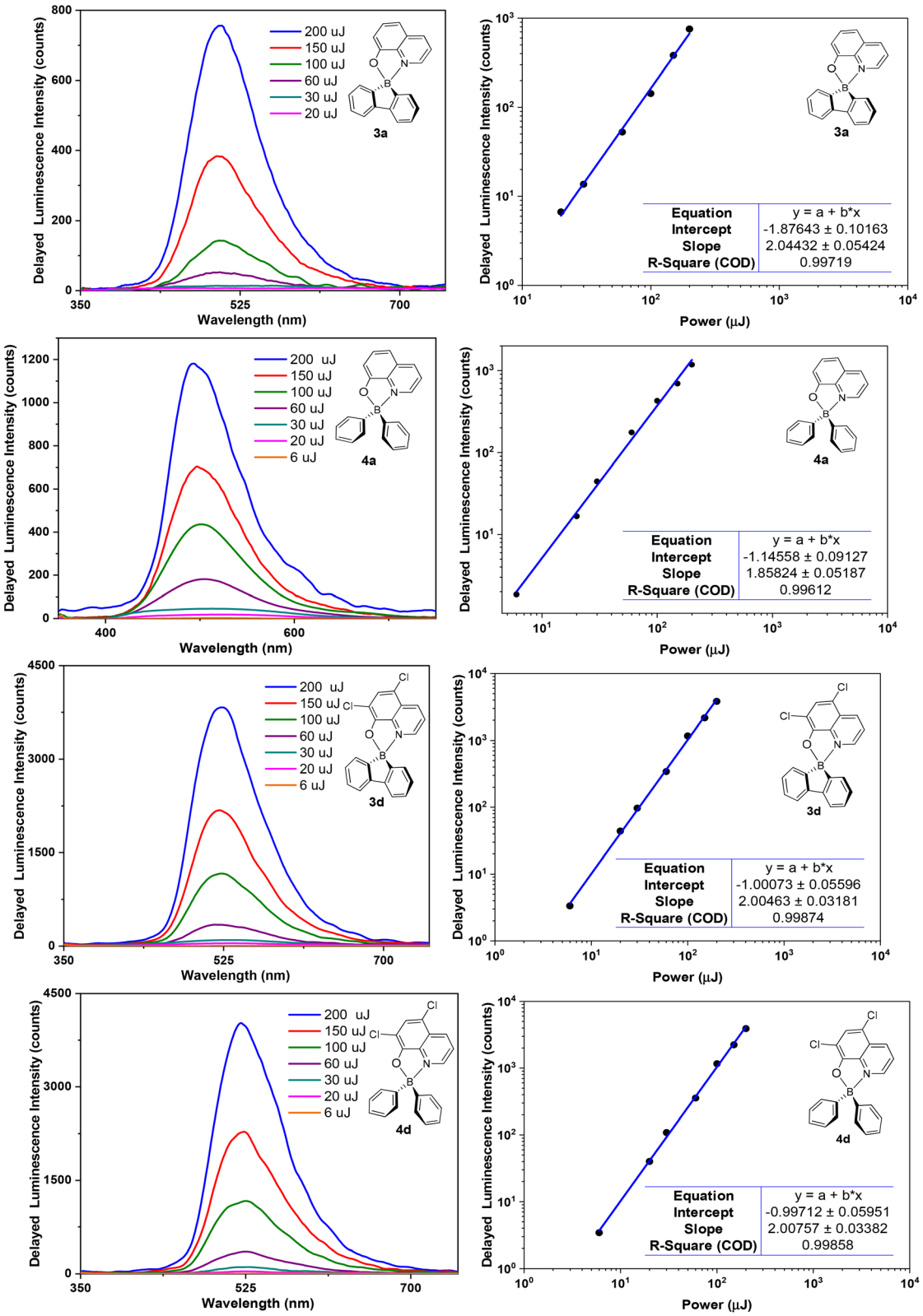

Fig. 7 Left: Dependence of DF intensity on the excitation dose for complexes **3a,d** and **4a,d** in ZEONEX 480R films at room temperature (*ca.* 293 K). Right: log–log plot of DF intensity as a function of excitation dose. A start delay (SD) of 20 μs was used.

Table 4 Characteristics of OLED devices based on complexes **3a**, **4a**, **3c**, **4c**, **3d**, and **4d**

Device	Emitter	V_{ON} [a] (V)	L_{max} [b] (cd m^{-2})	λ_{EL}^{max} [c] (nm)	CE_{max} [d] (cd A^{-1})	EQE_{max} [e] (%)	CIE 1931 [f] (x; y)
3a	**3a**	6.5	3600	490	6.0	2.4	(0.21; 0.41)
4a	**4a**	6.5	2600	488	6.2	2.6	(0.19; 0.37)
3a opt.	**3a**	6.0	6300	489	8.0	3.3	(0.21; 0.41)
4a opt.	**4a**	6.5	3800	489	7.4	2.9	(0.21; 0.41)
3c	**3c**	5.0	3500	503	6.4	2.5	(0.27; 0.50)
4c	**4c**	8.0	2400	501	8.3	2.6	(0.27; 0.51)
3d	**3d**	5.0	2700	502	6.5	2.2	(0.27; 0.50)
4d	**4d**	6.0	2400	499	5.8	2.0	(0.27; 0.50)

[a] Turn-on voltage at 10 cd m^{-2}. [b] Maximum luminance. [c] Electroluminescence spectrum maxima. [d] Maximum current efficiency. [e] Maximum external quantum efficiency. [f] Colour coordinates of the electroluminescence spectrum as defined in the International Commission on Illumination colour space CIE 1931.

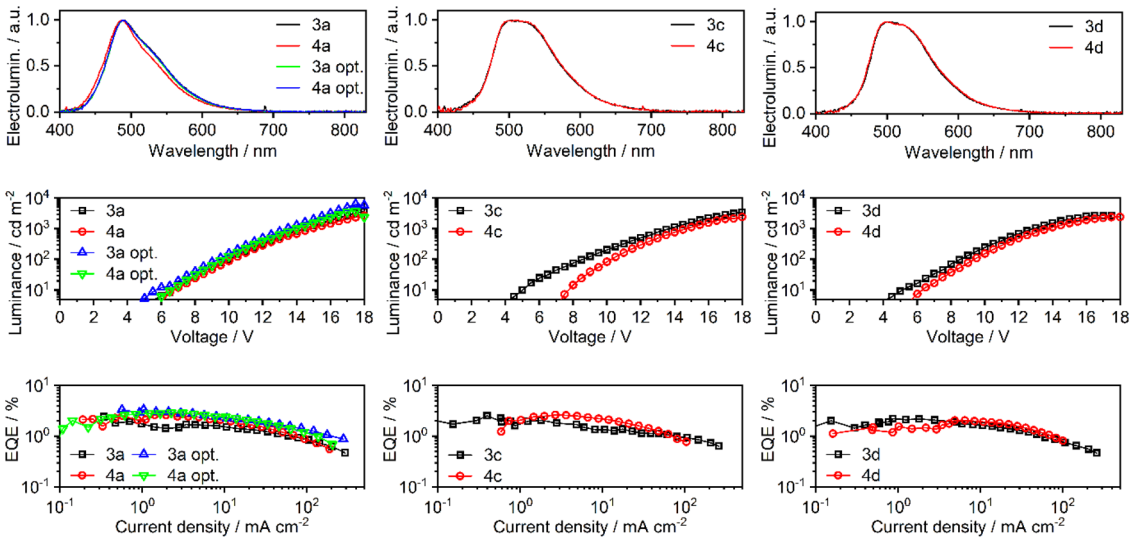

Fig. 8 Characteristics of OLED devices: electroluminescence spectra (top); luminance *vs.* voltage (middle); external quantum efficiency (EQE) *vs.* current density (bottom).

hole–electron balance within the emissive layer. The maximum EQE was *ca.* 3% while the maximum luminance reached 6300 cd m^{-2} and 3800 cd m^{-2}, respectively, for **3a opt.** and **4a opt.**

To demonstrate the effect of halogenation of the 8-quinolinolate ligand, a simpler structure of devices **3a**/**4a** was used as a basis for devices **3c**/**4c** and **3d**/**4d**. Addition of a single peripheral chlorine atom results in a change of the electroluminescence spectrum in devices **3c**/**4c**, which remains similar in **3d**/**4d** despite the second chlorine atom added to the emitter. Addition of one chlorine atom does not appear to affect the OLED performance as devices **3c**/**4c** display similar characteristics to **3a**/**4a**. OLEDs with two chlorines in the emitter molecule (**3d**/**4d**) display lower EQE and luminance than devices **3a**/**4a**, leading to reduced fluorescence efficiency. In this case the maximum EQE lowers to around 2.0–2.2%. While the respective **3x**/**4x** OLEDs display near identical electroluminescence spectra and similar EQE, it is evident that the **3x** devices present higher maximum luminance. Such behaviour is a resultant of the overall higher current density in the **3** series, suggesting that emitter structures **3x** have a lower negative effect on the carrier mobility of the emissive layer (*via* lower trapping) or a positive effect on charge injection.

All the presented OLED devices turn on at *ca.* 4 V, but only reach a luminance of 10 cd m^{-2} at around 5–8 V. Overall, the electroluminescence spectra of all devices are consistent with those recorded in a solution or a ZEONEX 480R film, being blue shifted and demonstrating a more resolved vibronic progression.

Conclusions

In summary, a family of six new 9-borafluoren-9-yl and diphenylboron complexes (**3b–d** and **4b–d**, respectively) containing halogen-substituted 8-quinolinolato *N*,*O*-bidentate ligands as second chromophores has been synthesised and structurally characterised. They display distorted tetrahedral geometries about the boron atom. These complexes are fluorescent exhibiting emission colours between green-blue and green-yellow.

Their photophysical study reveals film photoluminescence quantum yields (Φ_f) in the range of 0.06 to 0.26 and lifetimes (τ_f) of 10 to 24 ns, with the lower values corresponding to the more electronegative F-substituted complex **3b** and the higher ones to the Cl-disubstituted complex **3d**. Nevertheless, these values are smaller than those observed for the reference 8-quinolinolate unsubstituted derivative **3a** (0.39 and 28 ns).

The calculated absorption and emission energies reproduced very well the experimental energies. The nature of the $S_0 \rightarrow S_1$ transition ranged from 8-quinolinolato π–π* (intra-ligand) to mixed π–π* 8-quinolinolato and inter-ligand charge transfer in **3a** and monosubstituted **3b,c**. However, the transition in the Cl disubstituted **3d** complex exhibited only an inter-ligand charge transfer character between the orthogonal ligands.

Time-resolved luminescence measurements show that complexes **3a–d** and **4a–d** exhibit delayed fluorescence (DF) in ZEONEX 480R films. The mechanism behind this luminescence behaviour is demonstrated to be TTA rather than TADF, as evidenced by laser fluence experiments. We also argue that the calculated energy gap between S_1 and T_1 (ΔE_{ST}) of *ca.*1 eV, as calculated from DFT, is too large to consider TADF as the possible reason for the observed delayed fluorescence.

Finally, we fabricated organic light-emitting diode (OLED) devices displaying green-blue and green electroluminescence. The best performing OLED using emitter **3a** displays an external quantum efficiency (EQE) of 3.3% and a maximum luminance (L_{max}) of 6300 cd m^{-2}.

Experimental section

General

All experiments dealing with air- and/or moisture-sensitive materials were carried out under an inert atmosphere using a dual vacuum/nitrogen line and standard Schlenk and glovebox techniques.[32] Nitrogen gas was supplied by Air Liquide and purified by passage through 4 Å molecular sieves. Unless otherwise stated, all reagents were purchased from commercial suppliers (*e.g.* Acrös, Aldrich, Fluka, and Alfa Aesar) and used without further purification. All solvents to be used under an inert atmosphere were thoroughly deoxygenated and dehydrated before use. They were dried and purified by refluxing over a suitable drying agent followed by distillation under nitrogen. The following drying agents were used: sodium/benzophenone (for toluene, THF and diethyl ether) and calcium hydride (for *n*-hexane and dichloromethane). Solvents and solutions were transferred using a positive pressure of nitrogen through stainless steel cannulas and mixtures were filtered in a similar way using modified cannulae that could be fitted with glass fibre filter disks.

Nuclear magnetic resonance (NMR) spectra were recorded on a Bruker Avance III 300 spectrometer at 300.130 MHz (^{1}H), 75.468 MHz (^{13}C), 96.2712 MHz (^{11}B), and 282.404 (^{19}F) or on a Bruker Avance III 400 spectrometer at 400.130 MHz (^{1}H), 100.613 MHz (^{13}C), 128.3478 (^{11}B) and 376.498 (^{19}F). Deuterated solvents were dried by storage over 4 Å molecular sieves and degassed by the freeze–pump–thaw method. Spectra were referenced internally using the residual protio solvent resonance (^{1}H) and the solvent carbon resonance (^{13}C) relative to tetramethylsilane (δ = 0), and referenced externally using 15% $BF_3{\cdot}OEt_2$ (δ = 0) for ^{11}B, and $CFCl_3$ (δ = 0) for ^{19}F. The labelling of protons and carbons of the 9-borafluoren-9-yl and substituted 8-quinolinolato moieties of complexes **3** and **4** used in the NMR assignments of this work is given in Chart 2. All chemical shifts are quoted in δ (ppm) and coupling constants are given in hertz. Multiplicities are abbreviated as follows: singlet (s), doublet (d), doublet of doublets (dd), triplet (t), triplet of doublets (td) and multiplet (m). For air- and/or moisture-sensitive materials, samples were prepared in J. Young NMR tubes in a glovebox. Elemental analyses were obtained from the IST elemental analysis services.

The different 8-hydroxyquinolines (*i.e.* 8-quinolinols) were used as received and the reagents 9-chloro-9-borafluorene (**2**)[18] and BPh_3 [33] were prepared according to procedures reported in the literature.

Materials used for device fabrication were purchased from Sigma Aldrich {LiF (99.995%), TAPC}, Lesker {Al pellets (99.9995%)} and LUMTEC (TPBi, mCP, HAT-CN).

Syntheses

Synthesis of (κ²-*N*,*O*-8-quinolinolato)-9-borafluorene (3a). Complex **3a** has already been reported in the literature.[17] However, we herein present an improved and more convenient

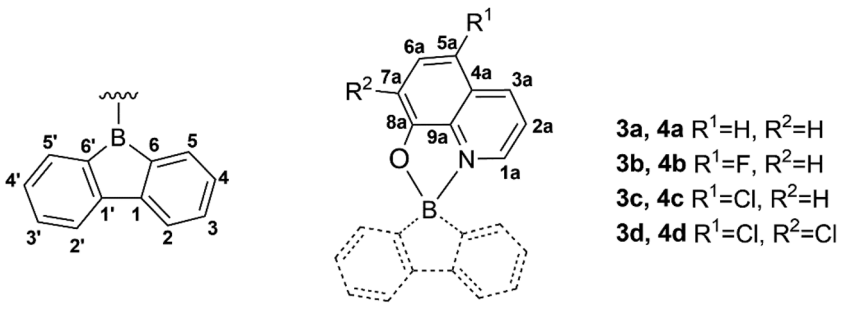

Chart 2 Labelling of protons and carbons of the 9-borafluoren-9-yl and substituted 8-quinolinolato moieties of complexes **3** and **4** used in the NMR assignments of this work.

synthetic procedure for complex **3a**, presenting an increased yield and avoiding the use of *tert*-butyl lithium and aqueous work-up: a solution of 8-hydroxyquinoline **1a** (0.26 g; 1.8 mmol), in tetrahydrofuran, was added to an excess of NaH (0.06 g; 2.3 mmol) at room temperature. The resulting yellow solution was stirred for 2 h and then filtered and added dropwise to a solution of 9-chloro-9-borafluorene **2** (0.35 g; 1.8 mmol) also in THF at a low temperature (−80 °C). The yellow solution was stirred overnight, under nitrogen, and allowed to slowly warm up to room temperature. On the next day, the solution was filtered and all the volatiles were removed under vacuum. A yellow powder of the desired product **3a** was obtained from an Et_2O solution kept at −20 °C for 2 h. Yield, 0.43 g (79%). ^{1}H NMR (300 MHz, CD_2Cl_2): δ 8.46 (d, $^3J_{HH}$ = 9 Hz, 1H, H_{1a}), 7.98 (d, $^3J_{HH}$ = 6 Hz, 1H, H_{3a}), 7.73 (t, $^3J_{HH}$ = 6 Hz, 1H, H_{6a}), 7.68 (d, $^3J_{HH}$ = 9 Hz, 2H, H_2 + $H_{2'}$), 7.52 (dd, $^3J_{HH}$ = 9 Hz, $^4J_{HH}$ = 6 Hz, 1H, H_{2a}), 7.36 (d, $^3J_{HH}$ = 6 Hz, 1H, H_{5a}), 7.29 (td, $^3J_{HH}$ = 9 Hz, $^4J_{HH}$ = 3 Hz, 2H, H_3 + $H_{3'}$), 7.18 (d, $^3J_{HH}$ = 9 Hz, 1H, H_{7a}), 7.12–7.02 (m, 4H, H_4 + $H_{4'}$ + H_5 + $H_{5'}$). ^{13}C{^{1}H} NMR (75 MHz, CD_2Cl_2): δ 159.4 (C_{8a}), 149.1 (C_6 + $C_{6'}$), 139.5 (C_{3a}), 139.3 (C_{1a}), 133.2 (C_{6a}), 130.1 (C_4 + $C_{4'}$), 129.2 (C_3 + $C_{3'}$), 127.5 (C_5 + $C_{5'}$), 123.6 (C_{2a}), 119.8 (C_2 + $C_{2'}$), 112.9 (C_{5a}), 109.7 (C_{7a}), C_{4a} + C_{9a} + C_1 + $C_{1'}$ resonance absent. ^{11}B NMR (96.29 MHz, CD_2Cl_2): δ 12.3. Anal. Calcd (%) for $C_{21}H_{14}NOB{\cdot}0.1Et_2O$: C, 81.71; H, 4.80; N, 4.45. Found: C, 81.68; H, 4.74; N, 4.58.

Synthesis of (κ²-*N*,*O*-5-fluoro-8-quinolinolato)-9-borafluorene (3b). A solution of 5-fluoro-8-hydroxyquinoline **1b** (0.16 g; 1.0 mmol), in tetrahydrofuran, was added to an excess of NaH (0.03 g; 1.5 mmol) at room temperature. The resulting yellow suspension was stirred for 2 h and added dropwise to a solution of 9-chloro-9-borafluorene (0.20 g; 1.0 mmol) also in THF at a low temperature (−80 °C). The yellow solution was stirred overnight, under nitrogen, and allowed to slowly warm up to room temperature. The solution was filtered and all the volatiles were removed under vacuum. An orange powder of the desired product **3b** was obtained from an Et_2O solution kept at −20 °C overnight. Yield, 0.25 g (77%). ^{1}H NMR (400 MHz, THF-d_8) δ 8.69 (d, $^3J_{HH}$ = 8.4 Hz, 1H, H_{1a}), 8.20 (d, $^3J_{HH}$ = 5.1 Hz, 1H, H_{3a}), 7.78–7.66 (m, 1H, H_{2a}), 7.62 (d, $^3J_{HH}$ = 7.6 Hz, 2H, H_5 + $H_{5'}$), 7.46 (dd, $^3J_{HH}$ = 11.1 Hz, $^3J_{FH}$ = 8.3 Hz, 1H, H_{6a}), 7.19 (t, $^3J_{HH}$ = 7.2 Hz, 1H, H_4 + $H_{4'}$), 7.06–6.87 (m, 5H, H_{7a} + H_3 + H_2 + H_2' + $H_{3'}$). ^{13}C{^{1}H} NMR (101 MHz, THF-d_8): δ 150.36 (d, $^3J_{CF}$ = 29.4 Hz, C_{4a}), 142.17 (C_{3a}), 134.34 (C_{1a}), 130.44 (C_3 + $C_{3'}$ or C_2 + $C_{2'}$), 129.30 (C_4 + $C_{4'}$), 127.63 (C_3 + $C_{3'}$ or C_2 + $C_{2'}$), 124.99 (C_{2a}), 120.01 (C_5 + $C_{5'}$), 116.53 (d, $^3J_{CF}$ = 20.7 Hz, C_{6a}), 107.95 (d, $^3J_{CF}$ = 6.4 Hz, C_{7a}) + C_{5a} + C_{9a} + C_{8a} + C_6 + $C_{6'}$ + C_1 + $C_{1'}$ resonance absent. ^{11}B NMR (128 MHz, THF-d_8) δ 11.0. ^{19}F NMR (282 MHz, THF-d_8) δ −140.33. Anal. Calcd (%) for $C_{21}H_{13}BFNO{\cdot}0.25Et_2O$: C, 76.88; H, 4.55; N, 4.08. Found: C, 76.84; H, 4.10; N 4.13.

Synthesis of (κ²-*N*,*O*-5-chloro-8-quinolinolato)-9-borafluorene (3c). A solution of 5-chloro-8-hydroxyquinoline **1c** (0.21 g; 1.1 mmol), in tetrahydrofuran, was added to an excess of NaH (0.04 g; 1.4 mmol) at room temperature. The resulting yellow suspension was stirred for 1 h, then filtered and added dropwise to a solution of 9-chloro-9-borafluorene **2** (0.24 g; 1.1 mmol) also in THF at a low temperature (−80 °C). The yellow solution was stirred overnight, under nitrogen, and allowed to slowly warm up to room temperature. On the next day, the solution was filtered and all the volatiles were removed under vacuum. Crystals suitable for X-ray diffraction studies of the desired product **3c** were obtained from an Et_2O solution kept at −20 °C, for 24 h. Yield, 0.29 g (76%). ^{1}H NMR (300 MHz, CD_2Cl_2): δ 8.67 (dd, $^3J_{HH}$ = 9 Hz, $^4J_{HH}$ = 3 Hz, 1H, H_{1a}), 8.06 (dd, $^3J_{HH}$ = 6 Hz, $^4J_{HH}$ = 1.5 Hz, 1H, H_{3a}), 7.76 (d, $^3J_{HH}$ = 9 Hz, 1H, H_{6a}), 7.68 (d, $^3J_{HH}$ = 9 Hz, 2H, H_2 + $H_{2'}$), 7.64 (t, $^3J_{HH}$ = 6 Hz, 1H, H_{2a}), 7.33–7.25 (m, 2H, H_5 + $H_{5'}$), 7.12 (d, $^3J_{HH}$ = 9 Hz, 1H, H_{7a}), 7.09–7.02 (m, 4H, H_3 + $H_{3'}$ + H_4 + $H_{4'}$). ^{13}C{^{1}H} NMR (75 MHz, CD_2Cl_2): δ 158.6 (C_{8a}), 149.4 (C_6 + $C_{6'}$), 140.3 (C_{3a}), 136.9 (C_{1a}), 132.4 (C_{6a}), 129.9 (C_4 + $C_{4'}$), 129.2 (C_5 + $C_{5'}$), 127.5 (C_3 + $C_{3'}$), 127.1 (C_{5a}), 124.4 (C_{2a}), 119.2 (C_2 + $C_{2'}$), 115.9 (C_{4a}), 109.8 (C_{7a}), C_{9a} + C_1 + $C_{1'}$ resonance absent. ^{11}B NMR (96.29 MHz, CD_2Cl_2): δ 12.9. Anal. Calcd (%) for $C_{21}H_{13}NOBCl$: C, 73.84; H, 3.84; N, 4.10. Found: C, 73.43; H, 3.95; N, 4.09.

Synthesis of (κ²-*N*,*O*-5,7-dichloro-8-quinolinolato)-9-borafluorene (3d). A solution of 5,7-dichloro-8-hydroxyquinoline **1d** (0.26 g; 1.2 mmol), in tetrahydrofuran, was added to an excess of NaH (0.04 g; 1.6 mmol) at room temperature. The resulting greenish black solution was stirred for 2 h, then filtered and added dropwise to a solution of 9-chloro-9-borafluorene (0.24 g; 1.2 mmol) also in THF at a low temperature (−80 °C). The greenish yellow solution was stirred overnight, under nitrogen, and allowed to slowly warm up to room temperature. The solution was filtered and all the volatiles were removed under vacuum. The solid was washed with Et_2O to obtain the desired product **3d** as a bright greenish yellow solid. Crystals suitable for X-ray diffraction studies of the desired product were obtained from a mixture of THF and CH_2Cl_2 solution at room temperature for 24 h. Yield, 0.38 g (84%). ^{1}H NMR (400 MHz, THF-d_8) δ 8.67 (d, $^3J_{HH}$ = 8.3 Hz, 1H, H_{1a}), 8.19 (d, $^3J_{HH}$ = 5.0 Hz, 1H, H_{3a}), 7.80 (s, 1H, H_{6a}), 7.68 (t, $^3J_{HH}$ = 6.9 Hz, 1H, H_{2a}), 7.61 (d, $^3J_{HH}$ = 7.6 Hz, 2H, H_5 + $H_{5'}$), 7.22 (t, $^3J_{HH}$ = 6.8 Hz, 2H, H_4 + $H_{4'}$), 7.03–6.95 (m, 4H, H_3 + H_2 + H_2' + $H_{3'}$). ^{13}C{^{1}H} NMR (101 MHz, THF-d_8): δ 155.62 (C_{8a}), 150.45 (C_6 + $C_{6'}$), 142.61 (C_{3a}), 139.62 (C_{4a}), 137.68 (C_{1a}), 133.05 (C_{6a}), 130.39 (C_3 + $C_{3'}$ or C_2 + $C_{2'}$), 129.67 (C_4 + $C_{4'}$), 127.80 (C_3 + $C_{3'}$ or C_2 + $C_{2'}$), 126.29 (C_{5a}), 125.09 (C_{2a}), 120.09 (C_5 + $C_{5'}$), 116.95 (C_{9a}), 114.36 (C_{7a}), C_1 + $C_{1'}$ resonance absent. ^{11}B NMR (128 MHz, THF-d_8) δ 12.8. Anal. Calcd (%) for $C_{21}H_{12}BCl_2NO$: C, 67.07; H, 3.22; N, 3.72. Found: C, 66.84; H, 3.15; N, 3.60.

Synthesis of (κ²-*N*,*O*-8-quinolinolato)diphenylboron (4a). This synthesis was adapted from the literature.[12] A solution of 8-hydroxyquinoline **1a** (0.36 g; 2.4 mmol), in toluene, was added dropwise to triphenylboron (0.59 g; 2.4 mmol) also in toluene at room temperature. The resulting yellow solution immediately turns into a suspension, which was stirred overnight under nitrogen. On the next day, the suspension was filtered and the resulting yellow solution was concentrated. A yellow powder of the desired product **4a** was obtained by double layering a toluene solution with *n*-hexane, which was

kept at −20 °C. The solution was filtered and the powder was dried under vacuum. Yield, 0.52 g (69%). ^{1}H NMR (300 MHz, CD_2Cl_2): δ 8.61 (d, $^3J_{HH}$ = 6 Hz, 1H, H_{1a}), 8.47 (d, $^3J_{HH}$ = 9 Hz, 1H, H_{3a}), 7.71–7.65 (m, 2H, H_{2a} + H_{6a}), 7.43–7.38 (m, 4H, B-Ph_2-H_{ortho}), 7.29 (d, $^3J_{HH}$ = 9 Hz, 1H, H_{5a}), 7.23 (m, 6H, B-Ph_2-H_{meta} + B-Ph_2-H_{para}), 7.16 (d, $^3J_{HH}$ = 6 Hz, 1H, H_{7a}). ^{13}C{^{1}H} NMR (75 MHz, CD_2Cl_2): δ 158.8 (C_{8a}), 139.9 (C_{1a}), 139.4 (C_{3a}), 133.2 (C_{6a}), 132.2 (B-Ph_2-C_{ortho}), 129.0 (B-Ph_2-C_{ipso}), 127.9 (B-Ph_2-C_{meta}), 127.2 (B-Ph_2-C_{para}), 123.4 (C_{2a}), 112.8 (C_{5a}), 109.7 (C_{7a}), C_{4a} + C_{9a} resonance absent. ^{11}B NMR (96.29 MHz, CD_2Cl_2): δ 11.9. Anal. Calcd (%) for $C_{21}H_{16}NOB{\cdot}0.15Et_2O$: C, 81.00; H, 5.51; N, 4.37. Found: C, 80.53; H, 5.07; N, 4.41.

Synthesis of (κ^2-*N*,*O*-5-fluoro-8-quinolinolato)-diphenylboron (4b). A solution of 5-fluoro-8-hydroxyquinoline **1b** (0.16 g; 1 mmol), in toluene, was added dropwise to triphenylboron (0.24 g; 1 mmol) also in toluene at room temperature. The resulting yellow solution was heated to reflux and stirred overnight under nitrogen. On the next day, the solution was cooled down and concentrated. A yellow powder of the desired product **4b** was obtained by double layering a toluene solution with *n*-hexane, which was kept at −20 °C. The solution was filtered and the powder was dried under vacuum. Yield, 0.16 g (49%). ^{1}H NMR (300 MHz, CD_2Cl_2) δ 8.66 (d, $^3J_{HH}$ = 5.1 Hz, 1H, H_{1a}), 8.59 (d, $^3J_{HH}$ = 8.4 Hz, 1H, H_{3a}), 7.78–7.67 (m, 1H, H_{2a}), 7.44–7.38 (m, 4H, B-Ph_2-H_{ortho}), 7.36 (d, $^3J_{HH}$ = 8.4 Hz, 1H, H_{6a}), 7.30–7.21 (m, 6H, B-Ph_2-H_{meta} + B-Ph_2-H_{para}), 7.04 (dd, $^3J_{HH}$ = 8.4, $^4J_{HF}$ = 3.4 Hz, 1H, H_{7a}). ^{13}C{^{1}H} NMR (75 MHz, CD_2Cl_2): δ 155.54 (d, $^4J_{CF}$ = 2.8 Hz, C_{8a}), 148.07 (d, $^1J_{CF}$ = 243.3 Hz, C_{5a}), 141.13 (C_{1a}), 134.20 (C_{3a}), 132.35 (B-Ph_2-C_{ortho}), 128.10 (B-Ph_2-C_{meta}), 127.52 (B-Ph_2-C_{para}), 123.83 (d, $^4J_{CF}$ = 1.7 Hz, C_{2a}), 119.58 (d, $^2J_{CF}$ = 23.7 Hz, C_{4a}), 116.46 (d, $^3J_{CF}$ = 20.7 Hz, C_{6a}), 108.25 (d, $^3J_{CF}$ = 6.5 Hz, C_{7a}), C_{9a} + B-Ph_2-C_{ipso} resonance absent. ^{11}B NMR (96.29 MHz, CD_2Cl_2): δ 12.5. ^{19}F NMR (282 MHz, CD_2Cl_2) δ −138.95. Anal. Calcd (%) for $C_{21}H_{15}BFNO$: C, 77.10; H, 4.62; N, 4.28. Found: C, 76.60; H, 4.63; N, 4.19.

Synthesis of (κ^2-*N*,*O*-5-chloro-8-quinolinolato)-diphenylboron (4c). A solution of 5-chloro-8-hydroxyquinoline **1c** (0.18 g; 1 mmol), in toluene, was added dropwise to triphenylboron (0.24 g; 1 mmol) also in toluene at room temperature. The resulting yellow solution was heated to reflux and stirred overnight under nitrogen. On the next day, the solution was cooled down to room temperature, concentrated, filtered, and stored at −20 °C, precipitating a microcrystalline yellow solid. The supernatant solution was filtered off and the solid was dried under vacuum, corresponding to the desired product **4c**. Yield, 0.19 g (56%). ^{1}H NMR (300 MHz, CD_2Cl_2): δ 8.66 (m, 2H, H_{1a} + H_{3a}), 7.77 (t, $^3J_{HH}$ = 6.6 Hz, 1H, H_{2a}), 7.72 (d, $^3J_{HH}$ = 8.1 Hz, 2H, H_{6a}), 7.47–7.35 (d, $^3J_{HH}$ = 6.0 Hz, 4H, B-Ph_2-H_{ortho}), 7.32–7.19 (m, 6H, B-Ph_2-H_{meta} + B-Ph_2-H_{para}), 7.09 (d, $^3J_{HH}$ = 8.4 Hz, 1H, H_{7a}). ^{13}C {^{1}H} NMR (75 MHz, CD_2Cl_2): 158.5 (C_{8a}), 140.9 (C_{1a} or C_{3a}), 138.6 (C_{5a}), 137.2 (C_{1a} or C_{3a}), 132.7 (C_{6a}), 132.4 (B-Ph_2-C_{ortho}), 128.2 (B-Ph_2-C_{meta}), 127.6 (B-Ph_2-C_{para}), 124.4 (C_{2a}), 110.1 (C_{7a}), C_{4a} + C_{9a} resonance absent. ^{11}B NMR (96.29 MHz, CD_2Cl_2): δ 12.3. Anal. Calcd (%) for $C_{21}H_{15}BClNO$: C, 73.40; H, 4.40; N, 4.08. Found: C, 73.30; H, 4.32; N, 3.97.

Synthesis of (κ^2-*N*,*O*-5,7-dichloro-8-quinolinolato)-diphenylboron (4d). A solution of 5,7-dichloro-8-hydroxyquinoline **1d** (0.22 g; 1 mmol), in toluene, was added dropwise to triphenylboron (0.24 g; 1 mmol) also in toluene at room temperature. The resulting green solution was heated to reflux and stirred overnight under nitrogen. On the next day, the solution was cooled down to room temperature, concentrated, filtered, and stored at −20 °C, precipitating a microcrystalline green solid. The green solid was further recrystallised from dichloromethane at −20 °C. The supernatant solution was filtered off and the solid was dried under vacuum, corresponding to the desired compound **4d**. Yield, 0.31 g (81%). ^{1}H NMR (300 MHz, CD_2Cl_2): δ 8.75–8.63 (m, 2H, H_{1a} + H_{3a}), 7.80 (t, $^3J_{HH}$ = 5.1 Hz, 1H, H_{2a}), 7.76 (s, 1H, H_{6a}), 7.45–7.34 (d, $^3J_{HH}$ = 6.0 Hz, 4H, B-Ph_2-H_{ortho}), 7.32–7.18 (m, 6H, B-Ph_2-H_{meta} + B-Ph_2-H_{para}). ^{13}C {^{1}H} NMR (75 MHz, CD_2Cl_2): 153.8 (C_{8a}), 142.1 (C_{1a}), 137.7 (C_{3a}), 133.0 (C_{6a}), 132.4 (B-Ph_2-C_{ortho}), 128.2 (B-Ph_2-C_{meta}), 127.8 (B-Ph_2-C_{para}), 124.4 (C_{2a}), C_{4a} + C_{5a} + C_{7a} + C_{9a} + B-Ph_2-C_{ipso} resonances absent. ^{11}B NMR (96.29 MHz, CD_2Cl_2): δ 12.7. Anal. Calcd (%) for $C_{21}H_{14}BCl_2NO{\cdot}0.125CH_2Cl_2$: C, 65.28; H, 3.70; N, 3.60. Found: C, 65.68; H, 3.56; N, 3.61.

X-ray diffraction

The crystallographic data for complexes **3b**, **3c**, **3d**, **4b** and **4d** were collected using graphite monochromated Mo-Kα radiation (λ = 0.71073 Å) on a Bruker AXS-KAPPA APEX II diffractometer equipped with an Oxford Cryosystem open-flow nitrogen cryostat, at 150 K, and the crystals were selected under an inert atmosphere, stored in polyfluoroether oil and mounted on a nylon loop. Cell parameters were retrieved using Bruker SMART software and refined using Bruker SAINT on all observed reflections. Absorption corrections were applied using SADABS.[34] Structure solution and refinement were performed using direct methods with the programs SIR2004,[35] SIR2014 [36] and SHELXL,[37] included in the package of programs WINGX-Version 2014.1.[38] All hydrogen atoms were inserted in idealised positions and allowed to refine riding on the parent carbon atom, with a C–H distance of 0.95 Å for aromatic H atoms and with U_{iso}(H) = 1.2U_{eq}(C). Graphical presentations were prepared with ORTEP-3.[38] The CIF file corresponding to the molecular structure of complex **3b** presented B-level alerts, which were associated with a high R_{int} (0.248). Due to the poor diffracting power/lack of unique data of the crystal and the corresponding data, although all the atoms were correctly assigned and no twinning or disorder was found, one larger than expected residual density maximum of 1.08 e Å^{-3} was present close to the boron atom after the completion of the structure refinement. Nevertheless, it was possible to undoubtedly solve the molecular structure. Data were deposited at CCDC under the deposition numbers 2234859 for **3b**, 2234860 for **3c**, 2234861 for **3d**, 2234862 for **4b** and 2234863 for **4d**.†

Computational studies

Density functional theory calculations[23] were performed using the Amsterdam density functional program package (ADF).[24]

The geometries of complexes **3a–d** and **4a–d** were modelled after those described above and optimised without symmetry constraints. The Vosko–Wilk–Nusair[39] local density approximation of the correlation energy and the PBE0 functional,[40,41] including spin-orbit coupling (SOPERT),[25] were used, considering solvent effects (THF) according to the COSMO model implemented in ADF. Relativistic effects were described with the ZORA approximation.[42] Triple ζ Slater-type orbitals (STO) were used to describe all the electrons of H, C, B, N, and F, augmented with one set of polarization functions (ADF TZP basis set). TDDFT[26] calculations were performed to calculate the absorption spectra, with the Tamm–Dancoff approximation (TDA),[43] and to optimise the geometries of the first excited singlet and triplet states. The absorption spectra were also calculated in a vacuum to check the role of the polarity of the medium. Unrestricted calculations were carried out for open shell complexes. The calculated fluorescence rate constants were the reciprocal of the excited singlet state lifetimes obtained from the SOPERT calculations (SO). Dipole moments were calculated for the ground state (S_0), for the Franck–Condon excited state after vertical excitation (S'_1) and before molecular relaxation (the same geometry as S_0 with the electronic configuration of S_1), and for S_1.

In order to compare the results of this work with previous ones, and to probe the role of dispersion, the calculations described above (model A) were repeated with the Grimme D3 correction[44] (A/D3), with the B3LYP functional[45] (method B), and B3LYP with the Grimme D3 correction (B/D3) with the same TZP basis set. Another older approach used Becke's exchange[46] and Perdew's[47] correlation functionals, with TZ2P (two sets of polarization functions) and a small core in the gas-phase (GP). The structure obtained under these conditions was used to calculate the energy of the HOMO and LUMO in THF and dichloromethane (DCM) with COSMO. The first singlet excited states were obtained by promotion of one electron from the HOMO to the LUMO, with the same spin (T_1) or opposite spins (S_1) followed by geometry optimisation. The results from these calculations are presented in the ESI.† Geometries and orbitals were visualised with Chemcraft.[48]

Spectroscopic measurements

Sample preparation, absorption and fluorescence measurements. Solutions of all complexes with an optical density (OD) of <0.2 at λ_{abs}^{max} ($c < 8 \times 10^{-5}$ M) were used. For solid state measurements, toluene solutions of each boron complex (concentration of 1 mg mL^{-1}) and ZEONEX® 480R (concentration of 100 mg mL^{-1}), in toluene, were blended at a ratio of 1% wt and drop-cast (~80 μL) at 30 °C on quartz slides to form thin films by evaporation of the solvent under a nitrogen atmosphere.

Measurements in THF solution were carried out as follows: absorption and fluorescence spectra of **3a–d** and **4a–d** solutions were recorded with an Agilent Cary 8454 UV-visible spectrophotometer and a SPEX Fluorolog 212I, respectively. The fluorescence spectra were collected with right angle geometry, in the S/R mode, and corrected for instrumental wavelength dependence. Fluorescence quantum yields were determined by comparison with the quantum yields of α-tetrathiophene (for compounds **3a** and **4a**) and α-pentathiophene (for compounds **3b–d** and **4b–d**) in dioxane at 25 °C.

Absolute fluorescence quantum yield measurements. An integrating sphere for absolute measurements was used to obtain the values for the fluorescence emission quantum yields (Φ_f) of the solid powdered samples, as recommended by the EPA.[49] A NIST calibration lamp was used to compute the correction curve of the integrating sphere/detection system. This is of utmost importance, for the correct calculation of fluorescence quantum yields, Φ_f. A 355 nm continuous laser (LaserTechnic, 10 mW) was used as the excitation source and neutral density filters to attenuate the excitation light whenever needed. The signals were collected from the integrating sphere by a collimating beam probe coupled to an optical fibre (fused silica), in this way assuring the connection to the monochromator entrance. A fixed monochromator (Andor, Shamrock 163) coupled to an ICCD detector (Andor, i-Star 720) with time gate capabilities was used in the accumulation mode.

The absolute fluorescence quantum yields were obtained using the following equation:

$$\Phi_f = (P_c - (1 - A) \times P_b)/A \times L_a \quad \text{with } A = (1 - L_c/L_b),$$

where A is the absorption coefficient, P_b is the light emitted by the sample after absorption of scattered excitation light, P_c is the light emitted by the sample after absorption of directly incident laser light, L_a is the total amount of excitation laser light, L_b is the scattered laser light, and L_c is the excitation light spectrum.

In many cases P_b is negligible and the equation simply becomes:

$$\Phi_f = P_c/(L_a - L_c)$$

Using this methodology, the Φ_f determinations of several standard fluorophores with a known quantum yield were performed for validation purposes. The agreement found between the Φ_f obtained by the absolute method and the reported literature values validates the photoluminescence quantum yields determined by this absolute approach.

Fluorescence lifetime determination. Fluorescence lifetimes were determined using Easylife VTM equipment from OBB Corporation (Birmingham, NJ, USA), with the lifetimes ranging from 100 ps to 3 μs. This technique uses pulsed light sources from different LEDs (365 nm in this case) and measures the fluorescence intensity at different time delays after the excitation pulse. In this case, 490 nm cut-off emission filters were used both for solution and solid samples, depending on the sample under study. The instrument response function was measured using a Ludox scattering solution. FelixGX software from OBB was used for fitting and analysis of the decay dynamics, 1 to 4 exponentials and also a lifetime distribution analysis,[49b,50] with the exponential series method (ESM).

Transient emission spectroscopy (TRS EMI). The transient emission measurements were performed using a pulsed N_2 laser at 337 nm (OBB, model 4500 with ~1 mJ per pulse) as an excitation source. A fixed monochromator (Andor, Shemrock 163) coupled to an ICCD detector (Andor, i-Star 720) with time gate capabilities and in the kinetics mode was used to detect the fluorescence, delayed fluorescence or phosphorescence signals. The available detection range was from 200 nm to 900 nm. The signals were collected using a collimating beam probe coupled to an optical fibre (fused silica) assuring in this way the connection to the monochromator entrance. The TRS EMI spectra of all compounds under study (ZEONEX 480R films) were acquired in short time or long time domains using suitable gate widths and start delay, as provided by the ICCD (with a minimum temporal gate of 2.2 ns and with 1024 × 128 pixels in all spectral ranges).

Further details of the use of this time resolved emission spectroscopic technique can be found in ref. 49.

Organic light-emitting diodes

OLEDs were fabricated by vacuum thermal evaporation. Pre-cleaned indium-tin-oxide (ITO) coated glass substrates with a sheet resistance of 20 Ω cm^{-2} and an ITO thickness of 100 nm were used. The substrates were first washed with acetone and then sonicated in acetone and isopropanol for 15 min. Substrates were dried with compressed air and transferred into an ozone-plasma generator for 6 min at full power. Thermally deposited layers were obtained using a Kurt J. Lesker Spectros II deposition system at 10^{-6} mbar base pressure. All organic materials and aluminium were deposited at a rate of 1 Å s^{-1}. The LiF layer was deposited at a rate of 0.1–0.2 Å s^{-1}. Characterisation of OLED devices was conducted in a 10 inch integrating sphere (Labsphere) connected to a Source Measure Unit (SMU, Keithley) and coupled with a spectrometer USB4000 (Ocean Optics). Further details are available in ref. 51. Devices of 4 × 2 mm pixel size were fabricated.

Substances used for OLED fabrication have been purchased from suppliers indicated in parentheses: HAT-CN – dipyrazino [2,3-*f*:2′,3′-*h*]quinoxaline-2,3,6,7,10,11-hexacarbonitrile (sublimed, LUMTEC); TSBPA – 4,4′-(diphenylsilanediyl)bis(*N*,*N*-diphenylaniline) (LUMTEC); mCP – 1,3-bis(carbazol-9-yl) benzene (sublimed, LUMTEC); PO-T2T – 2,4,6-tris[3-(diphenylphosphinyl)phenyl]-1,3,5-triazine (LUMTEC); TPBi – 1,3,5-tris (1-phenyl-1*H*-benzimidazol-2-yl)benzene, (sublimed, LUMTEC); LiF (99.995%, Sigma Aldrich); Al pellets (99.9995%, Lesker).

The fully thermally deposited OLEDs comprised a hole injection layer: HAT-CN, a hole transport layer: TSBPA, an exciton blocking layer: mCP, a hole blocking layer: PO-T2T and an electron transport layer: TPBi, an electron injection layer: LiF and a cathode: Al. The optimised emissive layer comprised a blend host: mCP (hole transport component) and PO-T2T (electron transport component) for a balanced carrier ratio and improved charge injection into the emitter.

Conflicts of interest

There are no conflicts of interest to declare.

Acknowledgements

We thank the Fundação para a Ciência e a Tecnologia (FCT) for financial support (project PTDC/QUI-QIN/31585/2017) and for a fellowship to C. B. F. (2021.05622.BD). Centro de Química Estrutural and Institute of Molecular Sciences (IMS), BioISI – Instituto de Biossistemas e Ciências Integrativas, Instituto de Telecomunicações, and IBB-Institute for Bioengineering and Biosciences acknowledge the FCT for financial support (respectively: projects UIDB/00100/2020, UIDP/00100/2020 and LA/P/0056/2020; UIDB/04046/2020 and UIDP/04046/2020; UIDB/50008/2020; and UIDB/04565/2020).

References

1 For example: (*a*) M. A. Baldo, D. F. O'Brien, Y. You, A. Shoustikov, S. Sibley, M. E. Thompson and S. R. Forrest, *Nature*, 1998, **395**, 151–154; (*b*) T. Sajoto, P. I. Djurovich, A. Tamayo, M. Yousufuddin, R. Bau, M. E. Thompson, R. J. Holmes and S. R. Forrest, *Inorg. Chem.*, 2005, **44**, 7992–8003; (*c*) S. Kappaun, C. Slugovc and E. J. W. List, *Int. J. Mol. Sci.*, 2008, **9**, 1527–1547; (*d*) C. S. Oh, C. W. Lee and J. Y. Lee, *Dyes Pigm.*, 2013, **98**, 372–376; (*e*) A. Tronnier, A. Risler, N. Langer, G. Wagenblast, I. Münster and T. Strassner, *Organometallics*, 2012, **31**, 7447–7452; (*f*) C. W. Lee and J. Y. Lee, *Adv. Mater.*, 2013, **25**, 596–600; (*g*) X.-C. Hang, T. Fleetham, E. Turner, J. Brooks and J. Li, *Angew. Chem., Int. Ed.*, 2013, **52**, 6753–6756; (*h*) S. Grigalevicius, D. Tavgeniene, G. Krucaite, D. Blazevicius, R. Griniene, Y.-N. Lai, H.-H. Chiu and C.-H. Chang, *Opt. Mater.*, 2018, **79**, 446–449; (*i*) Z. Zhong, X. Wang, Y. Ma, F. Peng, T. Guo, J.-X. Jiang, L. Ying, J. Wang, J. Peng and Y. Cao, *Org. Electron.*, 2018, **57**, 178–185; (*j*) G. Li, D. G. Congrave, D. Zhu, Z. Su and M. R. Bryce, *Polyhedron*, 2018, **140**, 146–157; (*k*) Y.-X. Hu, X. Xia, W.-Z. He, Z.-J. Tang, Y.-L. Lv, X. Li and D.-Y. Zhang, *Org. Electron.*, 2019, **66**, 126–135; (*l*) M.-C. Tang, M.-Y. Chan and V. W.-W. Yam, *Chem. Rev.*, 2021, **121**, 7249–7279; (*m*) H. Amouri, *Chem. Rev.*, 2023, **123**, 230–270.

2 (*a*) M. Aydemir, G. Haykir, F. Türksoy, S. Gümüş, F. B. Dias and A. P. Monkman, *Phys. Chem. Chem. Phys.*, 2015, **17**, 25572–25582; (*b*) K. Goushi, K. Yoshida, K. Sato and C. Adachi, *Nat. Photonics*, 2012, **6**, 253–258; (*c*) T.-T. Bui, F. Goubard, M. Ibrahim-Ouali, D. Gigmes and F. Dumur, *Beilstein J. Org. Chem.*, 2018, **14**, 282–308.

3 (*a*) R. Delorme and F. Perrin, *J. Phys. Rad. Ser.*, 1929, **10**, 177–186; (*b*) G. N. Lewis, D. Lipkin and T. T. Magel, *J. Am. Chem. Soc.*, 1941, **63**, 3005–3018; (*c*) C. Parker and C. Hatchard, *Trans. Faraday Soc.*, 1961, **57**, 1894–1904.

4 (*a*) H. Sternlicht, G. C. Nieman and G. W. Robinson, *J. Chem. Phys.*, 1963, **38**, 1326–1335; (*b*) Z. Yang, Z. Mao, Z. Xie, Y. Zhang, S. Liu, J. Zhao, J. Xu, Z. Chi and M. P. Aldred, *Chem. Soc. Rev.*, 2017, **46**, 915–1016; (*c*) N. Chitraningrum, T.-Y. Chu, P.-T. Huang, T.-C. Wen and T.-F. Guo, *Org. Electron.*, 2018, **62**, 505–510.

5 X. Qiao and D. Ma, *Mater. Sci. Eng., R*, 2020, **139**, 100519.

6 (*a*) T. J. Penfold, F. B. Dias and A. P. Monkman, *Chem. Commun.*, 2018, **54**, 3926–3935; (*b*) P. L. dos Santos, J. S. Ward, P. Data, A. S. Batsanov, M. R. Bryce, F. B. Dias and A. P. Monkman, *J. Mater. Chem. C*, 2016, **4**, 3815–3824; (*c*) F. B. Dias, T. J. Penfold and A. P. Monkman, *Methods Appl. Fluoresc.*, 2017, **5**, 012001; (*d*) A. Endo, M. Ogasawara, A. Takahashi, D. Yokoyama, Y. Kato and C. Adachi, *Adv. Mater.*, 2009, **21**, 4802–4806; (*e*) J. Gibson, A. Monkman and T. Penfold, *ChemPhysChem*, 2016, **17**, 2956–2961.

7 (*a*) D. Li, H. Zhang and Y. Wang, *Chem. Soc. Rev.*, 2013, **42**, 8416–8433; (*b*) D. Frath, J. Massue, G. Ulrich and R. Ziessel, *Angew. Chem., Int. Ed.*, 2014, **53**, 2290–2310; (*c*) D. Suresh and P. T. Gomes, Advances in Luminescent Tetracoordinate Organoboron Compounds, in *Advances in Organometallic Chemistry and Catalysis*, ed. A. J. L. Pombeiro, John Wiley & Sons, Inc., Hoboken, NJ, USA, 2014, ch. 36, pp. 485–492; (*d*) S.-F. Liu, Q. Wu, H. L. Schmider, H. Aziz, N.-X. Hu, Z. Popovic and S. Wang, *J. Am. Chem. Soc.*, 2000, **122**, 3671–3678; (*e*) H.-Y. Chen, Y. Chi, C.-S. Liu, J.-K. Yu, Y.-M. Cheng, K.-S. Chen, P.-T. Chou, S.-M. Peng, G.-H. Lee, A. J. Carty, S.-J. Yeh and C.-T. Chen, *Adv. Funct. Mater.*, 2005, **15**, 567–574; (*f*) C. C. Vidyasagar, B. M. M. Flores, V. M. Jiménez-Pérez and P. M. Gurubasavaraj, *Mater. Today Chem.*, 2019, **11**, 133–155; (*g*) Y.-L. Rao and S. Wang, *Inorg. Chem.*, 2011, **50**, 12263–12274; (*h*) Y. Wu, W. Yuan, H. Ji, Y. Qin, J. Zhang, H. Li, Y. Li, Y. Wang, Y. Sun and W. Liu, *Dyes Pigm.*, 2017, **142**, 330–339; (*i*) X. Li, P. Tang, T. Yu, W. Su, Y. Li, Y. Wang, Y. Zhao and H. Zhang, *Dyes Pigm.*, 2019, **163**, 9–16; (*j*) K. Dhanunjayarao, X. Mukundam, R. V. R. N. Chinta and K. Venkatasubbaiah, *J. Organomet. Chem.*, 2018, **865**, 234–238; (*k*) F. Yagishita, T. Kinouchi, K. Hoshi, Y. Tezuka, Y. Jibu, T. Karatsu, N. Uemura, Y. Yoshida, T. Mino, M. Sakamoto and Y. Kawamura, *Tetrahedron*, 2018, **74**, 3728–3733; (*l*) D. Wang, Y.-P. Wan, H. Liu, D.-J. Wang and G.-D. Yin, *Dyes Pigm.*, 2018, **149**, 728–735; (*m*) H. Zhang, C. Liu, J. Xiu and J. Qiu, *Dyes Pigm.*, 2017, **136**, 798–806; (*n*) D. Suresh, C. S. B. Gomes, P. T. Gomes, R. E. Di Paolo, A. L. Maçanita, M. J. Calhorda, A. Charas, J. Morgado and M. T. Duarte, *Dalton Trans.*, 2012, **41**, 8502–8505. Errata: *Dalton Trans.*, 2012, **41**, 14713 and *Dalton Trans.*, 2013, **42**, 16969; (*o*) D. Suresh, P. S. Lopes, B. Ferreira, C. A. Figueira, C. S. B. Gomes, P. T. Gomes, R. E. Di Paolo, A. L. Maçanita, M. T. Duarte, A. Charas, J. Morgado and M. J. Calhorda, *Chem. – Eur. J.*, 2014, **20**, 4126–4140; (*p*) D. Suresh, C. S. B. Gomes, P. S. Lopes, C. A. Figueira, B. Ferreira, P. T. Gomes, R. E. Di Paolo, A. L. Maçanita, M. T. Duarte, A. Charas, J. Morgado, D. Vila-Viçosa and M. J. Calhorda, *Chem. – Eur. J.*, 2015, **21**, 9133–9149; (*q*) D. Suresh, B. Ferreira, P. S. Lopes, P. Krishnamoorthy, C. S. B. Gomes, A. Charas, D. Vila-Viçosa, J. Morgado, M. J. Calhorda, A. L. Maçanita and P. T. Gomes, *Dalton Trans.*, 2016, **45**, 15603–15620; (*r*) P. Krishnamoorthy, B. Ferreira, C. S. B. Gomes, D. Vila-Viçosa, A. Charas, J. Morgado, M. J. Calhorda, A. L. Maçanita and P. T. Gomes, *Dyes Pigm.*, 2017, **140**, 520–532; (*s*) A. I. Rodrigues, C. A. Figueira, C. S. B. Gomes, D. Suresh, B. Ferreira, R. E. Di Paolo, M. J. Calhorda, D. de Sa Pereira, F. B. Dias, J. Morgado, A. L. Maçanita and P. T. Gomes, *Dalton Trans.*, 2019, **48**, 13337–13352; (*t*) A. I. Rodrigues, P. Krishnamoorthy, C. S. B. Gomes, N. Carmona, R. E. Di Paolo, P. Pander, J. Pina, J. S. Seixas de Melo, F. B. Dias, M. J. Calhorda, A. L. Maçanita, J. Morgado and P. T. Gomes, *Dalton Trans.*, 2020, **49**, 10185–10202; (*u*) P. Krishnamoorthy, A. I. Rodrigues, C. B. Fialho, C. S. B. Gomes, B. Ferreira, A. Charas, D. Vila-Viçosa, J. M. S. S. Esperança, P. Pander, F. B. Dias, M. J. Calhorda, A. L. Maçanita, J. Morgado and P. T. Gomes, *Inorg. Chem. Front.*, 2021, **8**, 3960–3983; (*v*) A. C. Murali, P. Nayak and K. Venkatasubbaiah, *Dalton Trans.*, 2022, **51**, 5751–5771.

8 (*a*) Y.-J. Shiu, Y.-C. Cheng, W.-L. Tsai, C.-C. Wu, C.-T. Chao, C.-W. Lu, Y. Chi, Y.-T. Chen, S.-H. Liu and P.-T. Chou, *Angew. Chem., Int. Ed.*, 2016, **55**, 3017–3021; (*b*) B. M. Bell, T. P. Clark, T. S. De Vries, Y. Lai, D. S. Laitar, T. J. Gallagher, J.-H. Jeon, K. L. Kearns, T. McIntire, S. Mukhopadhyay, H.-Y. Na, T. D. Paine and A. A. Rachford, *Dyes Pigm.*, 2017, **141**, 83–92; (*c*) Y.-J. Shiu, Y.-T. Chen, W.-K. Lee, C.-C. Wu, T.-C. Lin, S.-H. Liu, P.-T. Chou, C.-W. Lu, I.-C. Cheng, Y.-J. Lien and Y. Chi, *J. Mater. Chem. C*, 2017, **5**, 1452–1462; (*d*) K. Matsuo and T. Yasuda, *Chem. Commun.*, 2017, **53**, 8723–8726; (*e*) M. Stanoppi and A. Lorbach, *Dalton Trans.*, 2018, **47**, 10394–10398; (*f*) P. Li, H. Chan, S.-L. Lai, M. Ng, M.-Y. Chan and V. W.-W. Yam, *Angew. Chem., Int. Ed.*, 2019, **58**, 9088–9094.

9 S. S. Kothavale and J. Y. Lee, *Adv. Opt. Mater.*, 2020, **8**, 2000922.

10 (*a*) T. N. Singh-Rachford, A. Haefele, R. Ziessel and F. N. Castellano, *J. Am. Chem. Soc.*, 2008, **130**, 16164–16165; (*b*) F. Deng, A. J. Francis, W. W. Weare and F. N. Castellano, *Photochem. Photobiol. Sci.*, 2015, **14**, 1265–1270.

11 J. E. Douglass, *J. Org. Chem.*, 1961, **26**, 1312–1313.

12 Q. Wu, M. Esteghamatian, N.-X. Hu, Z. Popovic, G. Enright, Y. Tao, M. D'Iorio and S. Wang, *Chem. Mater.*, 2000, **12**, 79–83.

13 S. Kappaun, S. Rentenberger, A. Pogantsch, E. Zojer, K. Mereiter, G. Trimmel, R. Saf, K. C. Möller, F. Stelzer and C. Slugovc, *Chem. Mater.*, 2006, **18**, 3539–3547.

14 (*a*) J. Ugolotti, S. Hellstrom, G. J. P. Britovsek, T. S. Jones, P. Hunt and A. J. P. White, *Dalton Trans.*, 2007, 1425–1432; (*b*) Y. Nagata and Y. Chujo, *Macromolecules*, 2008, **41**, 2809–2813; (*c*) F. Cheng, E. M. Bonder, A. Doshi and F. Jäkle, *Polym. Chem.*, 2012, **3**, 596–600; (*d*) G. Wesela-Bauman, L. Jastrzębski, P. Kurach, S. Lulinski, J. Serwatowski and K. Woźniak, *J. Organomet. Chem.*, 2012, **711**, 1–9; (*e*) G. Wesela-Bauman, P. Ciećwierz, K. Durka, S. Luliński,

J. Serwatowski and K. Woźniak, *Inorg. Chem.*, 2013, **52**, 10846–10859.
15 Y. Cui, Q.-D. Liu, D.-R. Bai, W.-L. Jia, Y. Tao and S. Wang, *Inorg. Chem.*, 2005, **44**, 601–609.
16 K. Durka, I. Głowacki, S. Luliński, B. Łuszczyńska, J. Smętek, P. Szczepanik, J. Serwatowski, U. E. Wawrzyniak, G. Wesela-Bauman, E. Witkowska, G. Wiosna-Sałyga and K. Woźniak, *J. Mater. Chem. C*, 2015, **3**, 1354–1364.
17 M. Urban, K. Durka, P. Górka, G. Wiosna-Sałyga, K. Nawara, P. Jankowski and S. Luliński, *Dalton Trans.*, 2019, **48**, 8642–8663.
18 (*a*) P. C. J. Kamer, G. P. F. van Strijdonck, J. N. H. Reek and P. W. N. M. van Leeuwen, Hydroformylation and Hydroxycarbonylation of Alkenes; Formation of C–N and C–C Bonds, ed. W. A. Herrmann, in *Synthetic Methods of Organometallic and Inorganic Chemistry*, Georg Thieme Verlag Stuttgart, New York, 2002, vol. 10, ch. 2, p. 54; (*b*) S. Biswas, I. M. Oppel and H. F. Bettinger, *Inorg. Chem.*, 2010, **49**, 4499–4506.
19 (*a*) Z. M. Hudson and S. Wang, *Acc. Chem. Res.*, 2009, **42**, 1584–1596; (*b*) P. Chen, R. A. Lalancette and F. Jäkle, *Angew. Chem., Int. Ed.*, 2012, **51**, 7994–7998; (*c*) M. Halik, W. Wenseleers, C. Grasso, F. Stellacci, E. Zojer, S. Barlow, J. L. Bredas, J. W. Perry and S. R. Marder, *Chem. Commun.*, 2003, 1490–1491; (*d*) C. D. Entwistle and T. B. Marder, *Chem. Mater.*, 2004, **16**, 4574–4585; (*e*) C. D. Entwistle and T. B. Marder, *Angew. Chem., Int. Ed.*, 2002, **41**, 2927–2931; (*f*) R. Bernard, D. Cornu, J. P. Scharff, R. Chiriac and P. Miele, *Inorg. Chem.*, 2006, **45**, 8743–8748; (*g*) R. Bernard, D. Cornu, P. L. Baldeck, J. Caslavsky, J. M. Letoffe, J. P. Scharff and P. Miele, *Dalton Trans.*, 2005, 3065–3071; (*h*) F. Jäkle, *Chem. Rev.*, 2010, **110**, 3985–4022.
20 H. Höpfl, V. Barba, G. Vargas, N. Farfan, R. Santillan and D. Castillo, *Chem. Heterocycl. Compd.*, 1999, **35**, 912–927.
21 N. N. Greenwood and A. Earnshaw, *Chemistry of the Elements*, Elsevier Butterworth-Heinemann, 2nd edn, 1997.
22 S. Alvarez, *Dalton Trans.*, 2013, **42**, 8617–8636.
23 R. G. Parr and W. Yang, *Density Functional Theory of Atoms and Molecules*, Oxford University Press, New York, 1989.
24 (*a*) G. te Velde, F. M. Bickelhaupt, S. J. A. van Gisbergen, C. Fonseca Guerra, E. J. Baerends, J. G. Snijders and T. Ziegler, *J. Comput. Chem.*, 2001, **22**, 931–967; (*b*) C. Fonseca Guerra, J. G. Snijders, G. te Velde and E. J. Baerends, *Theor. Chem. Acc.*, 1998, **99**, 391–403; (*c*) *ADF2013, SCM, Theoretical Chemistry*, Vrije Universiteit, Amsterdam, The Netherlands, **https://www.scm.com**.
25 F. Wang and T. Ziegler, *J. Chem. Phys.*, 2005, **123**, 154102.
26 (*a*) S. J. A. van Gisbergen, J. A. Groeneveld, A. Rosa, J. G. Snijders and E. J. Baerends, *J. Phys. Chem. A*, 1999, **103**, 6835–6844; (*b*) A. Rosa, J. Baerends, S. J. A. van Gisbergen, E. van Lenthe, J. A. Groeneveld and J. G. Snijders, *J. Am. Chem. Soc.*, 1999, **121**, 10356–10365; (*c*) S. J. A. van Gisbergen, A. Rosa, G. Ricciardi and E. J. Baerends, *J. Chem. Phys.*, 1999, **111**, 2499–2507; (*d*) S. J. A. van Gisbergen, J. G. Snijders and E. J. Baerends, *Comput. Phys. Commun.*, 1999, **118**, 119–138; (*e*) J. Moussa, L.-M. Chamoreau, A. D. Esposti, M. P. Gullo, A. Barbieri and H. Amouri, *Inorg. Chem.*, 2014, **53**, 6624–6633.
27 For example: (*a*) L. F. Vieira Ferreira, J. C. Netto-Ferreira, I. V. Khmelinskii, A. R. Garcia and S. M. B. Costa, *Langmuir*, 1995, **11**, 231–236; (*b*) A. Belay, E. Libnedengel, H. K. Kima and Y.-H. Hwang, *Luminescence*, 2016, **31**, 118–126.
28 M. J. Calhorda, P. T. Gomes, C. B. Fialho and T. C. F. Cruz, unpublished results.
29 M. S. Islam, C. M. B. Cordeiro, M. J. Nine, J. Sultana, A. L. S. Cruz, A. Dinovitser, B. W.-H. Ng, H. Ebendorff-Heidepriem, D. Losic and D. Abbott, *IEEE Access*, 2020, **8**, 97204–97214.
30 M. Chapran, P. Pander, M. Vasylieva, G. Wiosna-Salyga, J. Ulanski, F. B. Dias and P. Data, *ACS Appl. Mater. Interfaces*, 2019, **11**, 13460–13471.
31 M. Vasylieva, P. Pander, B. K. Sharma, A. M. Shaikh, R. M. Kamble, F. B. Dias, M. Czichy and P. Data, *Electrochim. Acta*, 2021, **384**, 138347.
32 For example: (*a*) P. T. Gomes, M. L. H. Green and A. M. Martins, *J. Organomet. Chem.*, 1998, **551**, 133–138; (*b*) M. M. Marques, S. Fernandes, S. G. Correia, J. R. Ascenso, S. Caroço, P. T. Gomes, J. F. Mano, S. G. Pereira, T. Nunes, A. R. Dias, M. D. Rausch and J. C. W. Chien, *Macromol. Chem. Phys.*, 2000, **201**, 2464–2468; (*c*) R. Garçon, C. Clerk, J.-P. Gesson, J. Bordado, T. Nunes, S. Caroço, P. T. Gomes, M. E. Minas da Piedade and A. P. Rauter, *Carbohydr. Polym.*, 2001, **45**, 123–127; (*d*) V. Rosa, P. J. Gonzalez, T. Avilés, P. T. Gomes, R. Welter, A. C. Rizzi, M. C. G. Passeggi and C. D. Brondino, *Eur. J. Inorg. Chem.*, 2006, 4761–4769; (*e*) C. S. B. Gomes, P. T. Gomes and M. T. Duarte, *J. Organomet. Chem.*, 2014, **760**, 101–107.
33 R. Köster, P. Binger, W. Fenzl, E. R. Wonchoba and G. W. Parshall, *Inorg. Synth.*, 1974, **15**, 134–136.
34 G. M. Sheldrick, *SADABS, Program for Empirical Absorption Correction*, University of Göttingen, Göttingen, Germany, 1996.
35 M. C. Burla, R. Caliandro, M. Camalli, B. Carrozzini, G. L. Cascarano, L. De Caro, C. Giacovazzo, G. Polidori and R. Spagna, *J. Appl. Crystallogr.*, 2005, **38**, 381–388.
36 M. C. Burla, R. Caliandro, B. Carrozzini, G. L. Cascarano, C. Cuocci, C. Giacovazzo, M. Mallamo, A. Mazzone and G. Polidori, *J. Appl. Crystallogr.*, 2015, **48**, 306–309.
37 (*a*) SHELXL: G. M. Sheldrick, *Acta Crystallogr., Sect. C: Struct. Chem.*, 2015, **71**, 3–8; (*b*) C. B. Hübschle, G. M. Sheldrick and B. Dittrich, *J. Appl. Crystallogr.*, 2011, **44**, 1281–1284.
38 L. J. Farrugia, *J. Appl. Crystallogr.*, 2012, **45**, 849–854.
39 S. H. Vosko, L. Wilk and M. Nusair, *Can. J. Phys.*, 1980, **58**, 1200–1211.
40 M. Ernzerhof and G. Scuseria, *J. Chem. Phys.*, 1999, **110**, 5029–5036.
41 C. Adamo and V. Barone, *J. Chem. Phys.*, 1999, **110**, 6158–6170.
42 E. van Lenthe, A. Ehlers and E.-J. Baerends, *J. Chem. Phys.*, 1999, **110**, 8943–8953.

43 S. Hirata and M. Head-Gordon, *Chem. Phys. Lett.*, 1999, **314**, 291–299.
44 S. Grimme, *J. Comput. Chem.*, 2004, **25**, 1463–1473.
45 M. Reiher, O. Salomon and B. A. Hess, *Theor. Chem. Acc.*, 2001, **107**, 48–55.
46 A. D. Becke, *J. Chem. Phys.*, 1998, **109**, 2092–2098.
47 (*a*) J. P. Perdew, *Phys. Rev. B: Condens. Matter Mater. Phys.*, 1986, **33**, 8822–8824; (*b*) J. P. Perdew, Erratum: *Phys. Rev. B*, 1986, **34**, 7406–7406.
48 Chemcraft Program. **https://www.chemcraftprog.com/index.html**. January 2023.
49 (*a*) L. F. Vieira Ferreira, I. F. Machado, A. Gama, F. Lochte, R. P. Socoteanu and R. Boscencu, *J. Photochem. Photobiol., A*, 2020, **387**, 112152; (*b*) D. P. Ferreira, D. S. Conceicão, F. Fernandes, T. Sousa, R. C. Calhelha, I. C. F. R. Ferreira, P. F. Santos and L. F. Vieira Ferreira, *J. Phys. Chem. B*, 2016, **120**, 1212–1220; (*c*) A. Barbieri and G. Accorsi, *EPA Newsl.*, 2006, 26–34.
50 T. J. F. Branco, A. M. B. do Rego, I. F. Machado and L. F. Vieira Ferreira, *J. Phys. Chem. B*, 2005, **109**, 15958–15967.
51 D. de Sa Pereira, A. P. Monkman and P. Data, *J. Visualized Exp.*, 2018, e56593.